
This is an electronic reprint of the original article.
This reprint may differ from the original in pagination and typographic detail.

Ferreira, Pedro M.; Caçador, David; Machado, Miguel A.; Carvalho, Marta S.; Vilaça, Pedro; Sorger, Gonçalo; Farias, Francisco Werley Cipriano; Figueiredo, Arthur Ribeiro; Vidal, Catarina

Smart piezoelectric composite : impact of piezoelectric ceramic microparticles embedded in heat-treated 7075-T651 aluminium alloy

Published in:
International Journal of Mechanics and Materials in Design

DOI:
[10.1007/s10999-024-09731-7](https://doi.org/10.1007/s10999-024-09731-7)

Published: 01/02/2025

Document Version
Publisher's PDF, also known as Version of record

Published under the following license:
CC BY

Please cite the original version:
Ferreira, P. M., Caçador, D., Machado, M. A., Carvalho, M. S., Vilaça, P., Sorger, G., Farias, F. W. C., Figueiredo, A. R., & Vidal, C. (2025). Smart piezoelectric composite : impact of piezoelectric ceramic microparticles embedded in heat-treated 7075-T651 aluminium alloy. *International Journal of Mechanics and Materials in Design*, 21(1), 155-180. <https://doi.org/10.1007/s10999-024-09731-7>

This material is protected by copyright and other intellectual property rights, and duplication or sale of all or part of any of the repository collections is not permitted, except that material may be duplicated by you for your research use or educational purposes in electronic or print form. You must obtain permission for any other use. Electronic or print copies may not be offered, whether for sale or otherwise to anyone who is not an authorised user.



Smart piezoelectric composite: impact of piezoelectric ceramic microparticles embedded in heat-treated 7075-T651 aluminium alloy

Pedro M. Ferreira · David Caçador · Miguel A. Machado · Marta S. Carvalho · Pedro Vilaça · Gonçalo Sorger · Francisco Werley Cipriano Farias · Arthur Ribeiro Figueiredo · Catarina Vidal

Received: 15 August 2024 / Accepted: 15 October 2024 / Published online: 11 November 2024
© The Author(s) 2024

Abstract Significant advances have been made in material synthesis in the last two decades, with a focus on polymers, ceramics, metals, and smart materials. Piezoelectric-based smart materials generate an electric voltage in response to loads, enabling distributed monitoring in critical structural parts. Friction stir processing (FSP) is a versatile approach that can enhance material performance in various engineering fields. The primary objective of the current research

is to examine the sensorial properties of heat-treated AA7075-T651 aluminium plates that have been included with Lead Zirconate Titanate (PZT) and Barium Titanate (BT) particles via FSP. This study includes a comparative analysis of sensitivities with AA5083-H111 self-sensing material, metallographic and physicochemical characterization, and an assessment of the mechanical properties impacted by the incorporation of piezoelectric particles. The sensitivity of AA7075-PZT was found to be significantly higher than that of AA7075-BT. AA7075-PZT achieved a maximum sensitivity of $15.27 \times 10^{-4} \mu\text{V}/\text{MPa}$ while AA7075-BT had a sensitivity of only $7.28 \times 10^{-4} \mu\text{V}/\text{MPa}$, which is 52% lower. Microhardness and uniaxial tensile tests demonstrated that the presence of particles has an influence on both mechanical strength and electrical conductivity of aluminium components, as opposed to those that do not have particles. The complete investigation intends to give significant insights into the performance and prospective uses of these innovative smart materials, therefore advancing materials science and engineering.

P. M. Ferreira (✉) · D. Caçador · M. A. Machado · M. S. Carvalho · F. W. C. Farias · C. Vidal
UNIDEMI, Department of Mechanical and Industrial Engineering, NOVA School of Science and Technology, Universidade NOVA de Lisboa, 2829-516 Caparica, Portugal
e-mail: pdm.ferreira@campus.fct.unl.pt

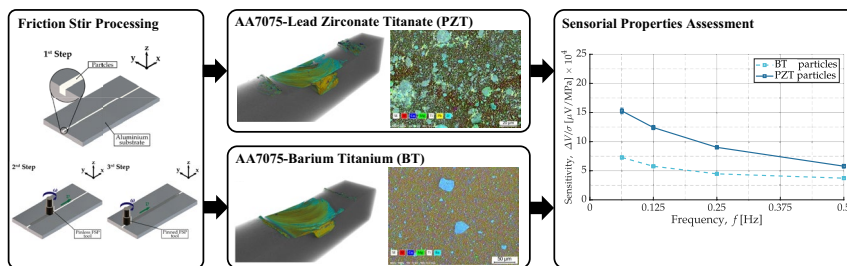
P. M. Ferreira
ESTSetúbal, Instituto Politécnico de Setúbal,
2910-761 Setúbal, Portugal

M. A. Machado · M. S. Carvalho · C. Vidal
Laboratório Associado de Sistemas Inteligentes, LASI,
4800-058 Guimarães, Portugal

P. Vilaça · G. Sorger
Department of Mechanical Engineering, School
of Engineering, Aalto University, P.O Box 14200,
00076 Espoo, Finland

A. R. Figueiredo
Program of Metallurgical and Materials Engineering,
Federal University of Rio de Janeiro (UFRJ),
Rio de Janeiro, RJ 21941-972, Brazil

Graphical abstract



Keywords Piezoelectric composite · Piezoelectric materials · Sensorial properties · Friction stir processing · Smart materials

1 Introduction

Over the last two decades, significant progress has been made in the field of materials synthesis, owing to scientific and technological advances. Notably, these materials may be divided into four categories: polymers, ceramics, metals, and smart materials (Hussain and Sia 2020; Bogue 2014). Smart materials, also known as shape memory, piezoelectric, pyroelectric, or thermoelectric materials, are composite materials that have been integrated with fiber optics, actuators, sensors, microelectromechanical systems, and functionalities like vibration control, sound control, shape control, product health monitoring, and intelligent processing (Rendas et al. 2023; Duarte et al. 2021; Santos et al. 2020; Mou et al. 2009; Ramanathan et al. 2022; Anton and Sodano 2007; Ferreira et al. 2022). Employing smart materials instead of conventional materials/methods for sensing and responding presents a transformative paradigm, simplifying devices, reducing weight, minimizing failure risks, and concurrently enhancing design flexibility, functionality, reproducibility, and reliability (Hussain and Sia 2020; Mateus et al. 2024a; Oyedepo et al. 2022). The integration of these intelligent materials holds great promise for fostering a more sustainable and energy-efficient world (Oyedepo et al. 2022; Mateus et al. 2024b). Various authors have proffered definitions to delineate smart materials. Lefebvre et al. (Smart materials: development of new sensory experiences through stimuli responsive materials. 2015) propose a

comprehensive definition, characterizing smart materials as those that dynamically alter their properties in response to stimuli, adapting to their environment. In contrast, Mekhzoum et al. (Mekhzoum et al. 2020) present a more exhaustive definition, emphasizing the ability to revert to the original state after stimulus removal, thus characterizing smart materials as both responsive and reversible (Sobczyk et al. 2022).

Efforts have been invested in categorizing these materials based on stimuli and response, elucidating their primary functionalities concerning material selection criteria (Das et al. 2021; Yanaseko et al. 2015, 2019). Furthermore, smart materials can be categorized as active or passive, contingent upon their capability to transduce energy. Active smart materials inherently possess the ability to transduce energy, while passive materials lack this intrinsic property. For instance, piezoelectric materials exemplify active smart materials, while fibre optics typify passive ones. Passive materials may serve as sensors but not as actuators (Mekhzoum et al. 2020).

Piezoelectric-based smart materials (PSM) are at the forefront of materials research and engineering, providing a one-of-a-kind combination of measuring simplicity and compatibility with data collecting systems. The intrinsic features of piezoelectric materials, which create an electric charge in reaction to mechanical stress, make them ideal for a wide range of applications, from structural health monitoring to wearable electronics (Ferreira et al. 2024a, b).

One of the key advantages of piezoelectric-based smart materials lies in their ability to provide spatially continuous sensing. Unlike traditional point-based sensors that only capture data at specific locations, these materials enable distributed sensing throughout their structure. This continuous

monitoring capability is especially valuable in applications where understanding variations and changes across an entire surface or structure is crucial (Das et al. 2021; Selleri et al. 2022), such as laminated (Xi and Chung 2019) or concrete structures (Sezer and Koç 2021). The name “piezoelectricity” is derived from the Greek terms “piezein” (to press) and “elektron,” which refers to amber, an ancient source of electric charge. In piezoelectric materials, each cell or molecule behaves as a dipole, having positive and negative charges at opposing ends. The alignment of these internal electric dipoles may produce a surface charge, which is balanced by free charges in the surrounding environment. The direct piezoelectric effect happens when an applied force deforms the material, changing its neutralized condition and producing an electric potential in response. Conversely, the converse piezoelectric effect transpires when an applied electric potential causes polarized molecules to align with the electric field, inducing deformation (Gohari et al. 2022; Scheffler and Poulin 2022).

These smart materials may be divided into two types: innately piezoelectric materials and designed materials containing piezoelectric fillers. Certain polymers and ceramics have intrinsic piezoelectric characteristics and do not require any extra changes. On the other hand, engineered materials involve the incorporation of piezoelectric fillers into non-piezoelectric matrices, expanding the range of material options available for specific applications (Sharma 2022; Askari et al. 2022). The versatility of piezoelectric-based smart materials is exemplified by their implementation in structural health monitoring. In this context, these materials can be embedded or integrated into structures such as bridges, buildings, or aircraft components. The continuous monitoring of mechanical stress and strain across these structures allows for early detection of potential issues, contributing to improved maintenance strategies and overall safety (Ferreira et al. 2023a, b).

Friction Stir Processing (FSP) has recently emerged as a viable technical solution for incorporating piezoelectric particles and creating materials with sensorial properties. For example, FSP was utilized to integrate BaTiO_3 and PbTiZrO_5 piezoelectric particles into an aluminium AA5083-H111 and AA2017-T451 plates, imparting sensorial properties (Ferreira et al. 2023a, 2024c; Wu et al. 2022; Khan et al. 2023).

FSP stands highlighted as a very promising surface modification technology due to its low cost and environmental friendliness (Vidal et al. 2023a; Liu et al. 2022; Rendas et al. 2024). The primary premise of FSP is to treat the base metal to extreme plastic deformation by vigorous stirring with a spinning instrument. One of the most significant advantages of FSP is its adaptability, which is not limited by the form of the workpiece or the processing environment (Dwivedi et al. 2023). Researchers have actively researched the enhancement of surface qualities using FSP by integrating second-phase particle materials, resulting in metal matrix composites (MMCs) (Vidal et al. 2023b; Moreira et al. 2023). This novel technique allows the creation of MMCs on chosen surfaces, resulting in bulk and surface characteristics that outperform those of metallic alloys (Inácio et al. 2022; Vidal et al. 2022). This unique feature distinguishes FSP as a disruptive technology with applications in a variety of sectors, including aerospace, automotive, marine, medicinal, and other technical areas. FSP’s capacity to improve durability and functionality makes it an appealing choice for enhancing material performance in a wide range of demanding applications, cementing its position as a significant innovation in surface modification technology (Sattari et al. 2018; Ragunath et al. 2024; Manroo et al. 2022).

Given FSP’s ability to incorporate sensitive particles into alloys commonly used in industry, the primary goal of the current work is to confer sensorial properties to heat-treated AA7075-T651 aluminium plates by incorporating Lead Zirconate Titanate (PZT) and Barium Titanium (BT) particles using FSP. To assess sensory qualities, their sensitivities will be compared to those of the AA5083-H111 self-sensing material under cyclic loading. Furthermore, the synthesized smart materials were metallographically and physiochemically characterized to study the impact of integrating particles inside the aluminium matrix. The mechanical characteristics were also investigated to assess the implication of adding these piezoelectric particles into the aluminium matrix. This detailed examination seeks to give insight into the performance and prospects.

Table 1 AA7075-T651 plates' chemical composition (wt%) (Inácio et al. 2022; Vidal et al. 2022)

Elements	Si	Fe	Cu	Mn	Mg	Cr	Zn	Ti	Al
Min	–	–	1.2	–	2.1	0.18	5.1	–	–
Max	0.4	0.5	2	0.3	2.9	0.28	6.1	0.2	Remaining

Table 2 AA7075-T651 plates' mechanical and physical properties (Inácio et al. 2022; Vidal et al. 2022)

Properties	AA7075-T651
Yield strength, $\sigma_{0.2}$ [MPa]	460
Modulus of elasticity, E [GPa]	71
Ultimate tensile strength, σ_{UTS} [MPa]	540
Vickers hardness [HV]	160

2 Materials and methods

2.1 Materials

PZT and BT particles were incorporated using FSP to provide sensorial properties to the heat-treated AA7075-T651 plates. The base plate, in the as-revied condition, underwent the T651 heat treatment, i.e., it was solution heated, stress relieved, and artificially aged (Inácio et al. 2022; Vidal et al. 2022). The

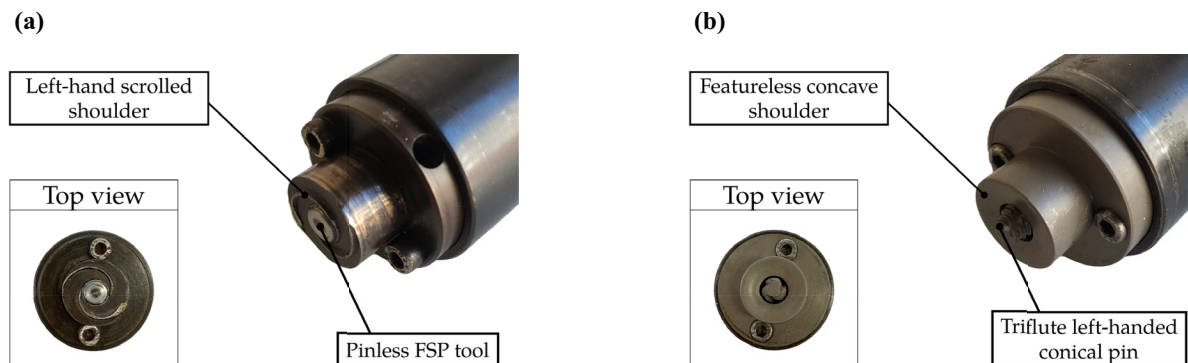
AA7075-T651 plates' chemical composition is presented in Table 1.

The main alloying elements in AA7075-T651 are magnesium (Mg) and zinc (Zn). Integrating these elements into 7xxx aluminum alloys improves mechanical strength and facilitates precipitation hardening. The PSM is made of AA7075-T651 plates that measure 203 (rolling direction) \times 103 \times 8 mm. Table 2 (Inácio et al. 2022; Vidal et al. 2022) summarizes the AA7075-T651 plates' mechanical and physical properties.

As previously stated, BT and PZT particles were added to aluminium base material to provide sensorial properties (Nanoshel 2024; TF Scientific 2024). The BT particles are 99.7% pure and have a homogeneous granular morphology, measuring less than 2 μ m. Prior investigations (Ferreira et al. 2023a, b, 2024c) used energy-dispersive X-ray spectroscopy to demonstrate the presence of oxygen, titanium, and barium, as expected. PZT particles are 99.9% pure

Table 3 BaTiO₃ and PbTiZrO₅' piezoelectric and physical properties (Ferreira et al. 2023a, b, 2024c)

Properties	BaTiO ₃	PbTiZrO ₅
Dielectric constant (K_{33})	1700	1300
Piezoelectric constant (d_{33} , d_{31}) [pC/N]	190, –78	270, –120
Electromechanical coupling coefficient (k_{33} , k_{31})	0.50, 0.21	0.71, –0.34
Curie temperature (T_c) [°C]	115	300–370

**Fig. 1** FSP tools: pinless tool **a**; pinned tool **b**

and range in size about to 20 μm . Unlike BT particles, PZT particles prefer to aggregate. Both BT and PZT are commercially accessible. Table 3 presents a comparison of the piezoelectric and physical characteristics of ceramic particles used.

2.2 Methods

The piezoelectric particles were embedded into the aluminium through FSP. The three-axis milling machine is used to produce the piezoelectric-based composite. The set of tools used is shown in Fig. 1 and includes a pinless FSP tool, chosen to ensure optimal particle distribution (Ferreira et al. 2023a, b, 2024c), and a pinned FSP tool. Both the pinless and pinned tool shoulders have a diameter of 19 mm. The pin has a conical shape with an angle of 14° and a bottom diameter of 5 mm.

The process parameters for incorporating these particles are already established and optimized according to the work developed by Ferreira et al. (2023a). Nevertheless, these parameters represent only a starting point since the processed base

material. To avoid the formation of defects and ensure the best particle distribution, adjustment of these parameters shall be considered to process the AA7075 plates.

Figure 2 shows three processes for embedding piezoelectric particles into plates. First, the piezoelectric particles are put and crushed into a single groove that has already been milled. The groove is then sealed, and particles are trapped with a single pass of the pinless FSP tool. Following that, four further passes are made in the same direction (X-direction), with no lateral movement (Y-direction), to obtain a more equal dispersion of particles throughout the nugget (Ferreira et al. 2023a, 2023b, 2024c).

During the processing of the plates, the temperature evolution was recorded using six equally spaced K-type thermocouples along the length of the aluminium plate, as illustrated in Fig. 3. The odd indices (T-K1, T-K3, T-K5) are referred to as the retreating side (RS), while even indices (T-K0, T-K2, T-K4) regard the advancing side (AS). To accommodate the thermocouples and ensure optimal contact between

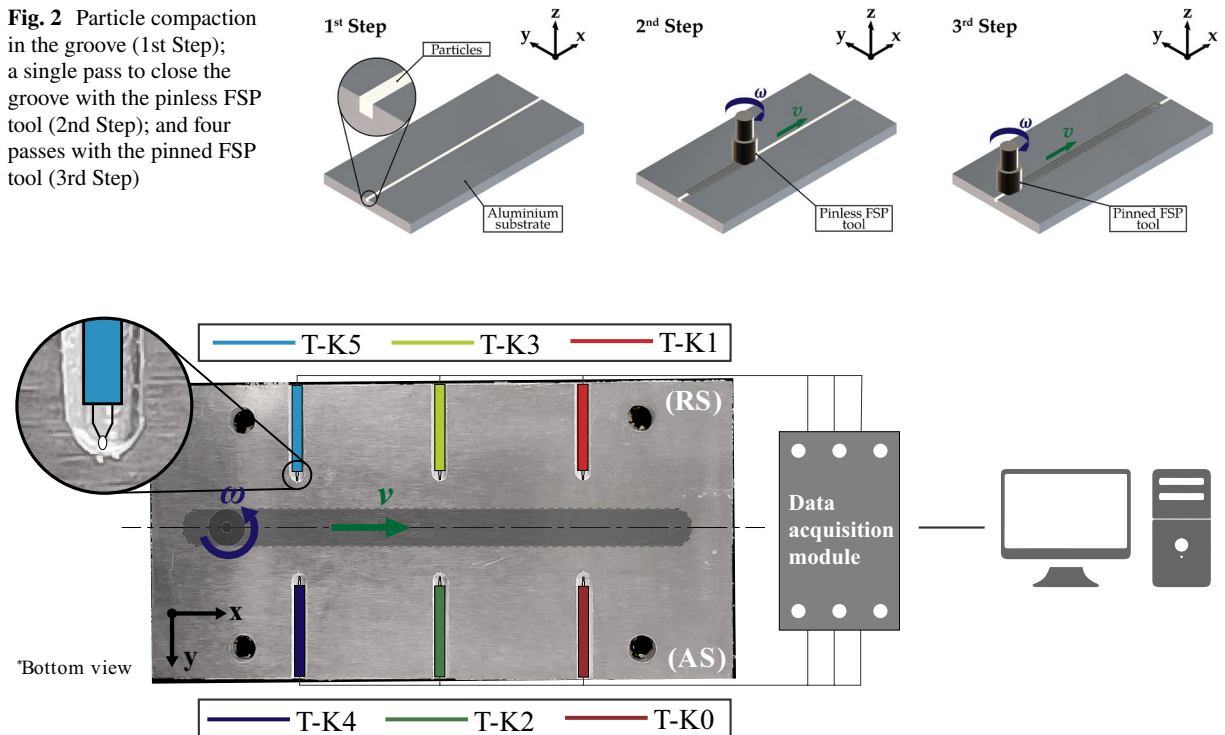


Fig. 3 Thermocouples' distribution along the plate

them and the plates during their processing, six grooves were previously machined.

The temperature data acquisition was made using the NI 9213 input module, installed in the NI-cDAQ-9178 CompactDAQ chassis from National Instruments. The data processing and recording were performed using LabView software. Additionally, the surface temperature of the plates was recorded during its processing using a Fluke Ti400 infrared thermal camera.

The top surfaces of the plates were painted black to prevent the reflection of infrared radiation emitted by the instrument, allowing for a more precise measurement of the temperatures involved during processing. The camera's emissivity was set to 0.95 for accurate temperature readings.

BT and PZT particles are perovskite-structured ferroelectric ceramics. Depending on the Curie temperature (T_c), this structure can be tetragonal, rhombohedral, orthorhombic, or cubic. Below T_c , BaTiO_3 transitions through tetragonal, orthorhombic, and rhombohedral phases, each with unique spontaneous polarization directions, creating an electrical dipole. Similarly, $\text{PbZr}_x\text{Ti}_{1-x}\text{O}_3$ typically presents tetragonal or rhombohedral phases below this temperature, exhibiting spontaneous polarisation. However, the exact phase depends on the specific composition of the material (Lines and Glass 1979). Above the Curie temperature, BaTiO_3 and $\text{PbZr}_x\text{Ti}_{1-x}\text{O}_3$ lose spontaneous polarization due to a symmetric lattice. Electrical dipoles cause deformation with an electric field (converse piezoelectric effect) or generate electrical displacement under strain (direct piezoelectric effect). These effects may not be visible macroscopically because dipoles are randomly arranged into domains.

Macroscopic effects need a preferential orientation of these domains, known as polarization. Thus, a polarisation process is performed by applying an electrical field (4.5 kV/mm) in a controlled environment (90 °C) for a duration of 2 h. This process ensures preferential alignment of the electric dipoles (Ferreira et al. 2023a, 2023b, 2024c). The electrical field (DC) is generated using an Oficel adjustable voltage generator. To regulate the temperature at which the polarisation is carried out, a digital-control power supply RS-3005D was used.

This procedure, depicted in Fig. 4, has proven to be very effective in increasing the electrical response of the PSM (Ferreira et al. 2023a, b, 2024c).

The production of the PSMs follows the procedures outlined in Fig. 2. It is intended to process both piezoelectric particles, i.e., BT and PZT. To perform all the characterisation techniques, two plates were produced for each type of piezoelectric particles. Additionally, a plate without particles was processed, to serve as a reference and evaluate the impact of adding the particles. Henceforth, the following nomenclature was adopted whenever there was a need to differentiate the processed plates: [Alloy]-[Piezoelectric particles]. For example, AA7075-BT refers to the first processed plate with BT particles in the AA7075 alloy. On the other hand, the processed plates without particles are denoted simply as AA7075-R.

2.3 Macro and microstructural characterization

A detailed macrostructural study of the PSMs was performed using an Olympus C×40 optical microscope to investigate the macrostructure and particle dispersion. All samples were immersed in epoxy

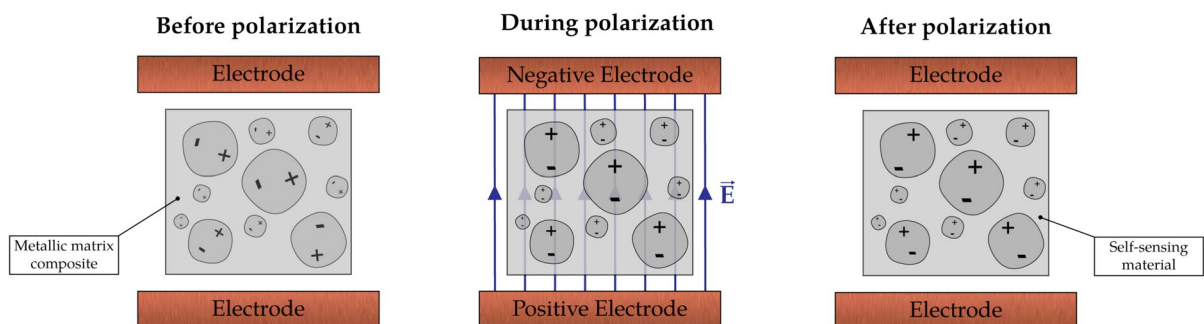


Fig. 4 Schematic of polarisation process

resin, ground, and polished using normal metallographic methods. The samples were etched using a Keller's reagent solution containing 175 ml of distilled water, 3 ml of HCl, 20 ml of HNO₃, and 2 ml of HF.

Using the inverted microscope Leica DMI 5000 M, the microstructure and distribution of the particle in the nugget where the piezoelectric particles were implanted were also examined and characterised in detail. The scanning electron microscopy (SEM) and energy dispersive X-ray spectroscopy (EDX) studies were carried out using a Zeiss Merlin VP Compact SEM with a Bruker XFlash EDX detector. The acceleration voltage was 15 kV, and the working distance was around (Mateus et al. 2024a; Smart materials: development of new sensory experiences through stimuli responsive materials. 2015) mm. The specimens were prepared using a Struers Tegramin automated polisher with a final grinding comparable to a 1200 grit paper, followed by polishing with 1 µm and 25 µm diamond suspension.

PSM samples were analysed using X-Ray Diffraction (XRD) on a PANalytical X'Pert Pro MDP diffractometer equipped with a Co K α anode and a 1D X'Celerator detector. The XRD data was analysed using High Score Plus software after continuous scanning from 20–90° (2 θ).

The materials' 3D micro-architectural morphology was analysed using X-ray microtomography (μ CT) on a Phoenix VITOMEIX GE system, as described by Vidal et al. (Vidal et al. 2022). The picture data was analysed subjectively and quantitatively with 3D tomographic reconstruction and Volume Graphics 3.04 software.

2.4 Mechanical and electrical characterization

At room temperature, uniaxial tensile tests were executed with a servo-hydraulic MTS 312.21 testing machine that has a 100 kN load capability, according to the ASTM E8/E8M-13a standard. The test specimens were fabricated using a HAAS Super Mini Mill 2 CNC Machining Center based on the geometry detailed by Ferreira et al. 2023a). These specimens were accurately machined to a consistent thickness of 2 mm revealing the nugget. The fracture surfaces were then examined with a Hitachi High-Tech SU3800 Scanning Electron Microscope. The

tensile tests were designed to evaluate and describe the mechanical behaviour of the PSMs.

The specimens were also meticulously prepared for further investigation, and the Vickers microhardness profile was measured along their length (Y direction) with a Mitutoyo HM-112 microhardness testing equipment. This method followed ASTM E384—10 guidelines. The spacing between successive indentations was fixed at 1 mm for the base material and lowered to 0.5 mm for processing and thermal/mechanical impacts. A standardized load of 1.0 kgf was applied for 10 s for the microhardness testing. The purpose of these measurements was to define both the processed and unprocessed zones of the samples, as well as to quantify particle dispersion within the PSMs.

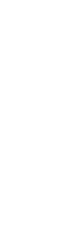
Eddy current and potential drop measuring methods were used to evaluate the samples' electrical conductivity, as described in Sorger et al. (2019); Santos et al. 2011). The measurements were taken in a straight line in the Y direction. A pencil probe with a frequency of 1.0 MHz was utilized in conjunction with a NORTEC 600 D impedance analyzer for the eddy current approach. A Jandel™ linear four-point probe with four tungsten needles with 40 µm tip radius and 0.635 mm spacing was used for potential drop measurements. A Keithley Nanovoltmeter 2182A was used to monitor the voltage between the two inner needles, and an external current of 80 mA was delivered to the outer needles using a Keithley SourceMeter 2450.

The mechanical strength can be evaluated by hardness measurements because hardness is directly proportional to mechanical behaviour of PSM. The resistivity and conductivity of both processed and unprocessed zones was analysed by potential drop measurements. Thus, hardness and mechanical behaviour are inversely related to electrical conductivity, as demonstrated by certain authors (Sorger et al. 2019; Santos et al. 2011). The eddy current testing was used to investigate microstructural changes in the material (Sorger et al. 2019; Santos et al. 2011).

2.5 Sensorial properties assessment

To illustrate the material's inherent self-sensing capabilities due to the existence of piezoelectric particles, a number of laboratory tests were carried out to

Table 4 Processing parameters optimization for AA7075-T451

Processing parameters	1st Pass	2nd Pass	3rd Pass	4th Pass
$v = 71$ mm/min	—			
$\omega = 1120$ rev/min	—			
$v = 90$ mm/min	—			
$\omega = 1120$ rev/min	—			
$v = 112$ mm/min	—			
$\omega = 1120$ rev/min	—			



analyse its electrical response under cyclic loadings. Cyclonic loads were applied using an MTS 312.21 testing equipment. The uniaxial tensile specimens were subjected to cyclic loading with fifteen tensile cycles at higher frequencies (f , 0.063, 0.125, 0.250, and 0.500 Hz). Several different cyclic load intensities were used. The load intensity was regulated by displacement (X direction), with amplitudes A set at 0.02, 0.03, 0.04, 0.05, 0.06, 0.07, 0.08, 0.09, and 0.10 mm.

A load cell was used to quantify the force caused by the cyclic loads during data collecting. The sample and the monitoring system were connected electrically, allowing direct contact with the sample surface. A Keithley Nanovoltmeter 2182A coupled to a National Instruments DAQ system was used to measure the electrical voltage response, which was then processed using a LabView application. All testing methods took place at ambient temperature.

The gain factor of Keithley Nanovoltmeter 2182A was configured at 9000, with a measurement range set to 0.01 mV, and no offset was applied. In essence, the Model 2182A exhibits a speed vs. noise profile reminiscent of a parabola. Specifically designed to excel in the 1 PLC to 5 PLC (power line cycles) reading range, this model stands out in the lowest noise region on the graph. Within this range, the Model 2182A not only addresses its internal drift through corrections but also maintains a swift response time, settling a step response in less than 100 ms. Consequently, the nanovoltmeter's rate setting was established at 5 PLC, which is the default option for the acquisition equipment. The number of power line cycles (PLC) serves as an indicator of the duration over which an input signal is integrated to yield a single measurement. Given the periodic nature of noise introduced from the power line, aligning the A/D converter's integration time with one cycle of this noise allows for the effective cancellation of signal components associated with the periodic interference. In general terms, extending the integration time by the A/D converter results in a more precise reading outcome, as it enables the cancellation of signal components from the periodic noise to a greater extent. In this sequence, the effect of the number of PLCs chosen on the acquired electrical voltage response was also evaluated.

Table 5 Processing parameters employed for PSMs' production

Processing parameters	Groove closing	1st–4th Pass
Rotation speed, ω [rev/min]	1400	1120
Travel speed, v [mm/min]	90	90
Tilt angle, [°]	1	1

3 Results and discussion

3.1 Sensitivity analysis of processing parameters

A sensitivity analysis of processing parameters was undertaken to optimize the distribution of particles. This examination of key processing variables was driven by the overarching goal of achieving the most desirable and consistent particle distribution.

To achieve this, the travel speed (v) was adjusted at 71, 90, and 112 mm/min. The travel speed was selected based on the discrete adjustment available in the FSP equipment used to produce the PSM. Meanwhile, the rotation speed was maintained at 1120 rev/min. Tables 4 and 5 show cross-sectional micrographs produced for the treated portions of the AA7075 alloys.

After carefully inspecting the cross-sections of the processed areas, flaws with a distinct linear shape may be seen in the nugget's bottom part, on the advancing side. However, the defects identified in the

macrographs are the result of a mismatch between the tool pin used for processing and the plates' groove.

Based on the results presented in Table 4, it was evident that performing at least four passes with the pinned tool enhances the distribution of particles within the nugget. For the study of this PSM, ensuring the optimal distribution of particles is crucial, which is achieved with a minimum of four passes. Comparing the macrographs of samples subjected to two and four passes with the pinned tool, a significant improvement in particle distribution within the nugget is observed, along with a reduction in areas of high ceramic particle concentration. So, optimal parameters for distributing particles in AA7075 are 90 mm/min and 1120 rev/min, respectively the travel and rotation speed, based on surface quality, particle distribution, and defect occurrence during processing. The ideal groove closing parameters for AA7075 are 90 mm/min and 1400 rev/min, respectively the travel and rotation speed. To successfully seal the groove, the rotation speed must be increased to 1400 rev/min, resulting in a larger material flux on the plate's surface.

3.2 Temperature measurements

Figure 5 displays the typical temperature evolution during a processing pass and the thermocouples' measurements during the third pass of the 7075-PZT plate. As expected, the right-sided (X-direction)

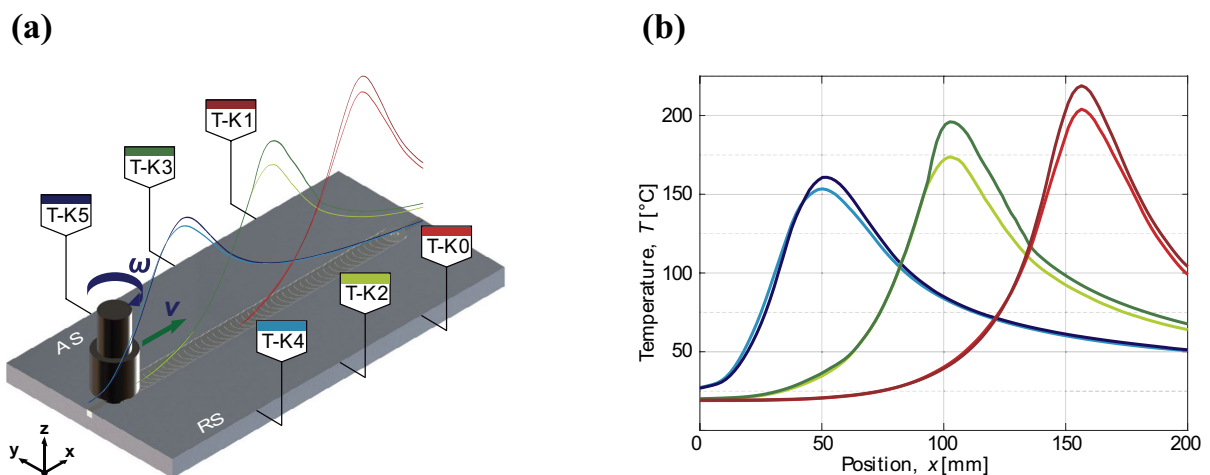


Fig. 5 Temperature evolution during processing: schematic thermocouples' distribution **a**; temperature measurements during the third pass of 7075-PZT **b**

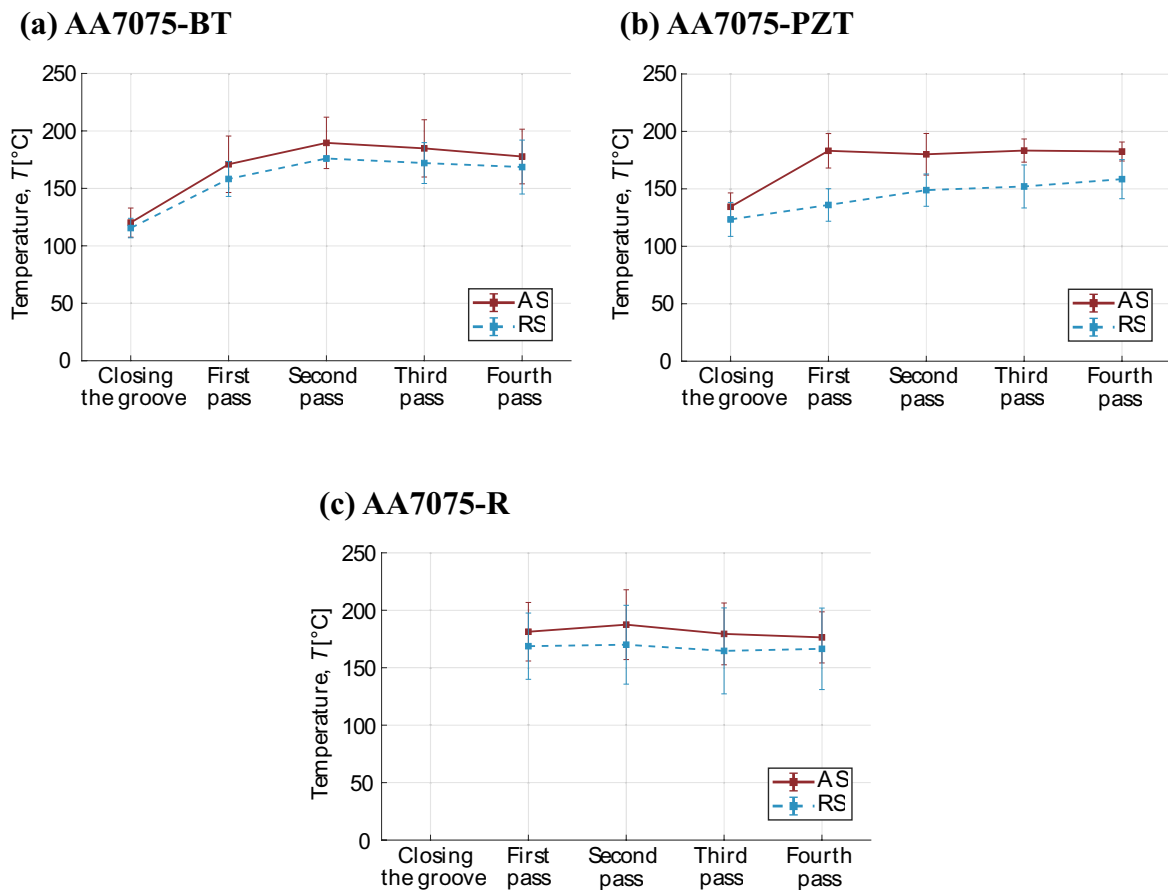


Fig. 6 Maximum temperatures of each pass registered by the thermocouples

thermocouples register successively higher temperature values since the FSP tool contributed to the global heating of the plate in an immediate prior instance. It may also be deduced that the temperature on the advancing side (AS) is greater than on the retreating side (RS), as predicted by Wu et al. (2019). In other words, the travel speed aligns with both the direction and sense of the tangential speed of the tool on the advancing side. This alignment leads to greater plastic deformation, resulting in increased heat generation and a subsequent rise in temperature on the advancing side compared to the retreating side. On the retreating side, while the travel speed shares the same direction, it differs in sense from the tangential speed of the tool.

Figure 6 depicts the maximum temperatures of each pass registered by the thermocouples at the advancing and retreating side while tool pin process the aluminium plate with and without piezoelectric

particles. According to same authors (Ferreira et al. 2023a), utilizing various embedding piezoelectric particles for the same base material results in no significant changes in maximum temperature. However, when the plates are processed without particles vs with particles, it is clear that the highest temperatures reported are somewhat greater in the later scenario.

All temperature measurements show that greater temperatures have been recorded on the advancing side. The observed occurrence is caused by a considerable increase in the production of heat., which principally originates from the simultaneous alignment of the material flux and the travel speed in the same direction.

The temperature achieved in the nugget is higher than that reached in the bottom region of the plate, where the thermocouple is located, hence the temperature measurements acquired from the thermocouple merely show how temperatures evolution.

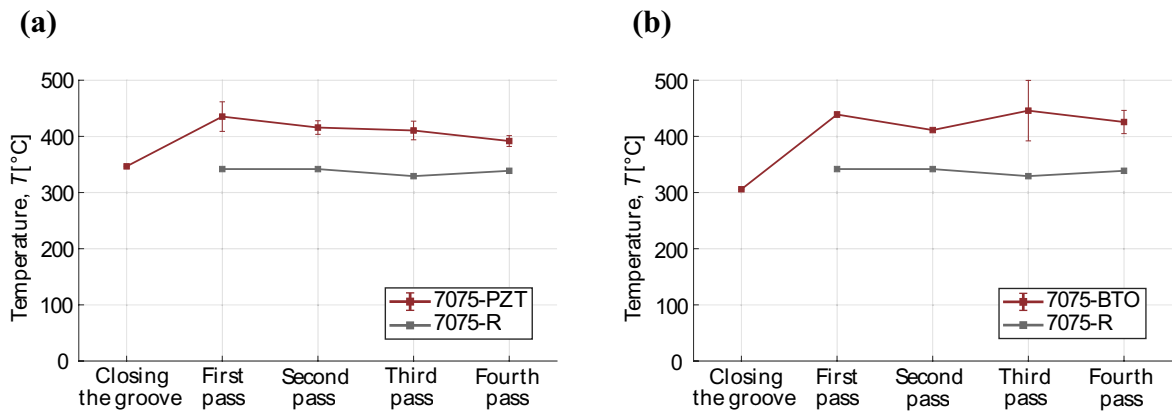


Fig. 7 Maximum temperatures of each pass registered by the thermal camera

Therefore, an IR camera was used to record the temperature on the plate surface and near the tool pin during processing. The highest temperatures recorded on the surface of the stir zones are presented in Fig. 7. The temperatures measured by the thermal camera are higher than those recorded by the thermocouples. This outcome was expected, as the thermocouples are distributed and positioned beneath the plate, while the thermal camera detects the temperature directly in the stir zone.

This is because the pinless FSP tool causes substantially less plastic deformation, i.e., reduced heat generation, than the pinned FSP tool. That is, lower temperature values, around 350 °C for the AA7075-PZT plate and 300 °C for the AA7075-BT plate. Additionally, an insignificant temperature variation is observed over the four processing passes, leading to the conclusion that the number of passes has little effect on the processing temperature.

Incorporating particles into the processing matrix complicates matters, necessitating additional energy to efficiently distribute and embed them. This is because when ceramic particles are added to the aluminium matrix via FSP, they act as a barrier to the heat conduction resulting from the FSP, hindering the thermal flow of the process. This results in an increase in local temperature due to the particles' low thermal conductivity (Parumandla and Adepu 2018; Su et al. 2003). As a result, higher temperatures are seen during particle processing, which implies more energy dissipation and greater resistance to deformation.

3.3 Characterisation of piezoelectric-based smart materials

3.3.1 Metallographic characterisation

Macro and microstructural characterisation techniques were used to analyse particle distribution within the processed zone, i.e. the nugget, as well as the heat-affected zone (HAZ) and the thermo-mechanically affected zone (TMAZ). Figure 8 macro- and micrographs of the AA7075 PSM samples.

It can be shown that FSP was successful in promoting particle dispersion in the aluminium matrix alloy. Ferreira et al. (2023a) previously conducted an EDX investigation for AA5083-H111 PSM and discovered that darker spots inside the stir zone have larger quantities of piezoelectric particles. As a result, processing AA7075 can be seen in darker spots where particles concentrate. Furthermore, the macrographs reveal that the particles are more equally dispersed in the AS than in the RS.

The macrographs where the shoulder has a greater impact, particularly the AA7075-BT plate (shown in Fig. 8e–h)), show a less homogenous distribution of particles inside this region, with larger clusters and some even display processing flaws. The specimens tested for uniaxial and sensorial behaviour have a thickness of 2 mm, which excludes the stir zone. The AA7075-PZT macrograph indicated two separate zones inside the pin-influenced zone. In contrast to the bottom region's micrograph, which shows smaller and more evenly distributed (see Fig. 8c, d).

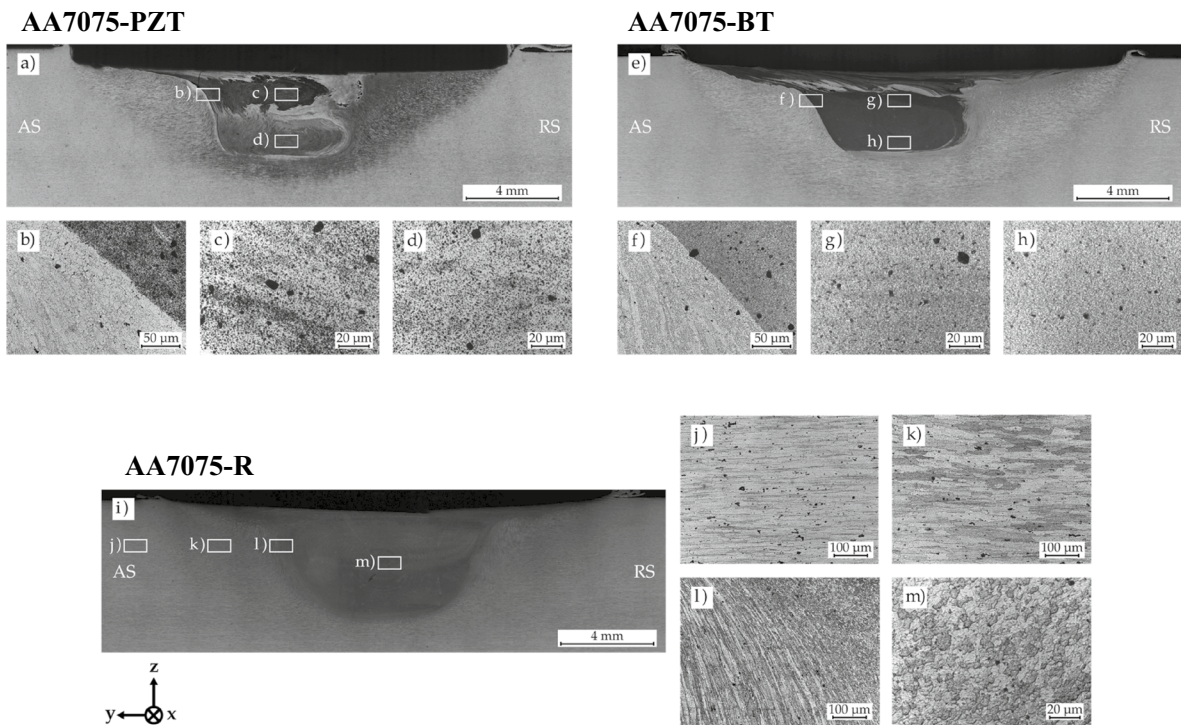


Fig. 8 Macro and microstructural characterisation of PSM—AA7075

Figure 8i–m) depicts the microstructural areas of aluminium processing without the particle. The heat created during the operation causes the HAZ to have bigger grains than the base material. The TMAZ shows how heat and extreme strain cause grain elongation and deformation. The stir zone demonstrates dynamic recrystallization because the material suffers high plastic deformation at high temperatures, which results in grain refinement.

The particle integration resulted in more dramatic grain refining in the AA7075 alloy when compared to the grain size inside the stir zone of a samples obtained without particles inclusion. The usage of reinforcement particles has already been examined to play a key function (Vidal et al. 2023b; Inácio et al. 2022).

Micrographs of the stir zone of PSMs treated with PZT demonstrated the existence of more and bigger particle agglomerates than the BT embedment. This trend is attributed to the fact that PZT particles are more irregular in shape and significantly larger (by an order of magnitude) compared to BT particles. This difference in particle size and shape influences

the grain size within the stir zone, as smaller particles generally lead to greater grain refinement compared to larger particles (Vidal et al. 2023b).

Figure 9 shows the EDX maps of the zones with piezoelectric particles in the AA7075-PZT specimen. As previously stated, the AA7075-PZT sample has two different zones inside the stir zone. Figure 9 shows SEM images that follow the micrographs provided earlier in Fig. 8, indicating that the top region has a less homogenous distribution of particles with bigger agglomerates, whereas the bottom region is more homogeneous and has smaller agglomerations. Figure 9a, b) shows EDX maps of both locations, which corroborate the variations in particle distribution.

Point spectrum analyses were conducted in both regions and are presented in Fig. 9c, d). In the upper region (Zone 1), higher magnification SEM reveals large agglomerates of PZT particles (Fig. 9d). Regarding the lower region (Zone 2), particle 1 has the chemical composition (wt%) of an expected PZT particle. Particle 2 which is slightly brighter under the SEM, appears to be either a precipitate given the

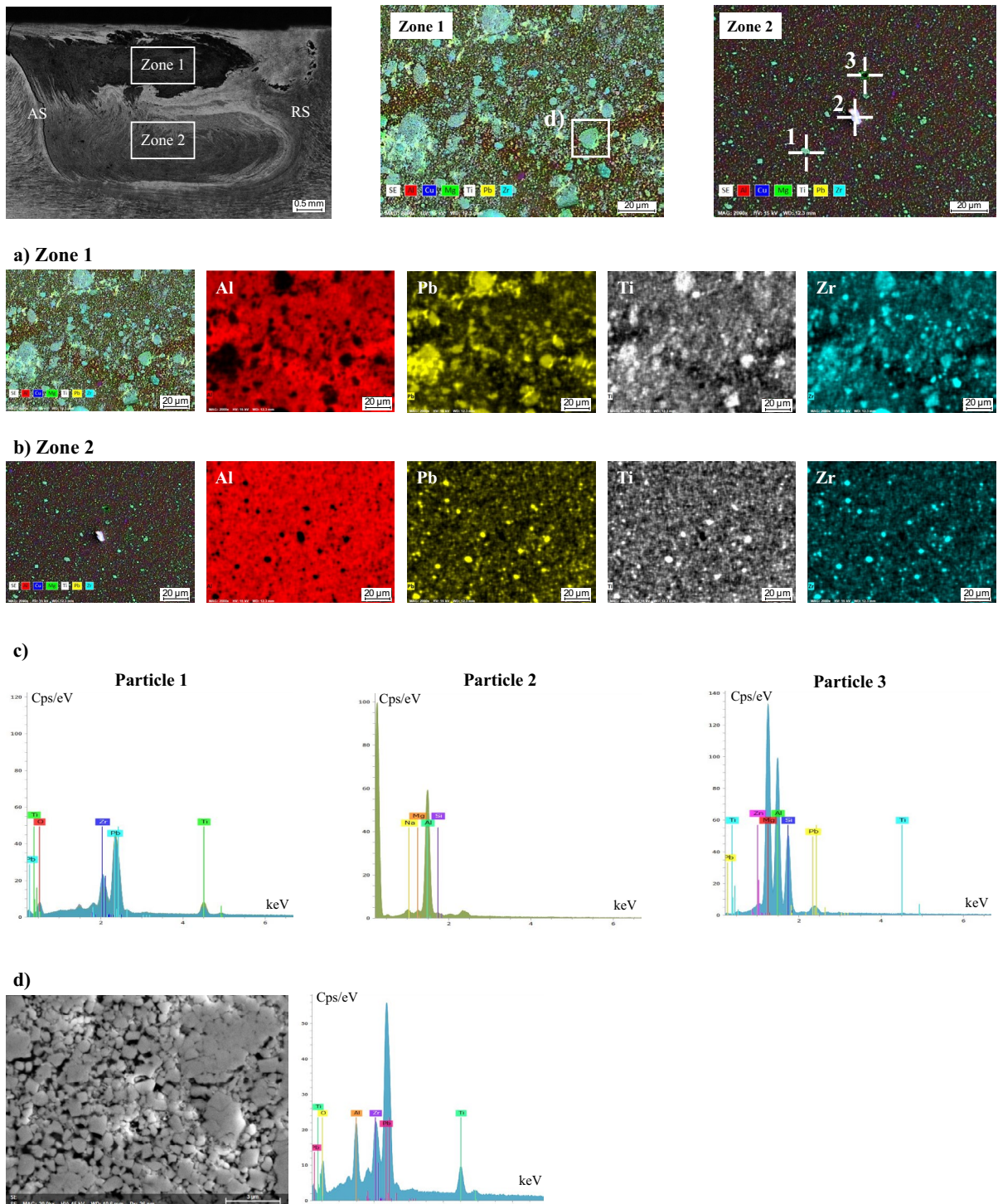


Fig. 9 SEM and EDX characterisation of particles' distribution of AA7075-PZT in distinct regions inside the nugget: upper region (Zone 1); lower zone (Zone 2), at $\times 2000$ magnification. EDX maps of Zone 1 **a** and Zone 2 **b** inside the nugget,

at $\times 2000$ magnification. **c** Point spectrum graphics of different particles found inside the stir zone (Zone 2). **d** SEM image of particles' agglomerate inside Zone 2 of the nugget and the respective spectrum graphic

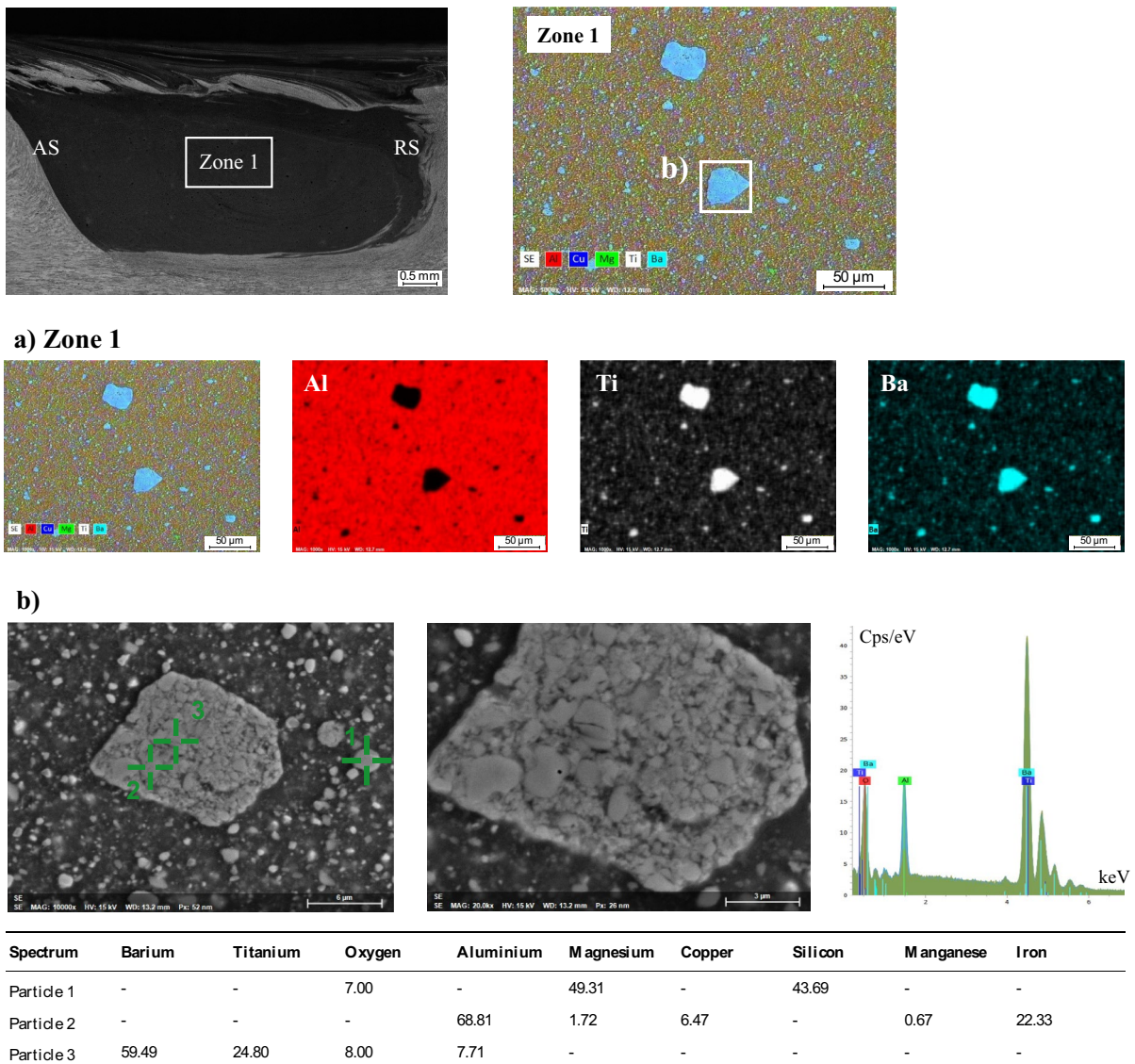


Fig. 10 SEM and EDX characterisation of particles’ distribution of AA7075-BT in zone influenced by the pin: **a** EDX maps of Zone 1, at $\times 1000$ magnification; **b** SEM image of par-

ticles’ agglomerate inside Zone 1 of the nugget and the respective spectrum graphic

presence of silicon, magnesium and aluminium, and the dark appearance of particle 3 could be another precipitate with high traces of silicon, magnesium, and aluminium.

Regarding the embedding of BT particles in AA7075, SEM and EDX analysis confirmed the presence of some sizeable agglomerates at low magnification, as evidenced in Fig. 10. Despite this, the overall distribution of particles is relatively homogeneous.

Point spectrum analysis were conducted on a smaller agglomerate, depicted in Fig. 10b. The chemical composition (wt%) shows evidence that particles 2 and 3, present inside the agglomerate, might be, a BT particle. In contrast, the nearby particle 1 could be a precipitate, given its high content of silicon and magnesium.

SEM analyses and EDX maps of the central region of the nugget of AA7075-R sample with point spectrum analysis are depicted in Fig. 11. The particle 1

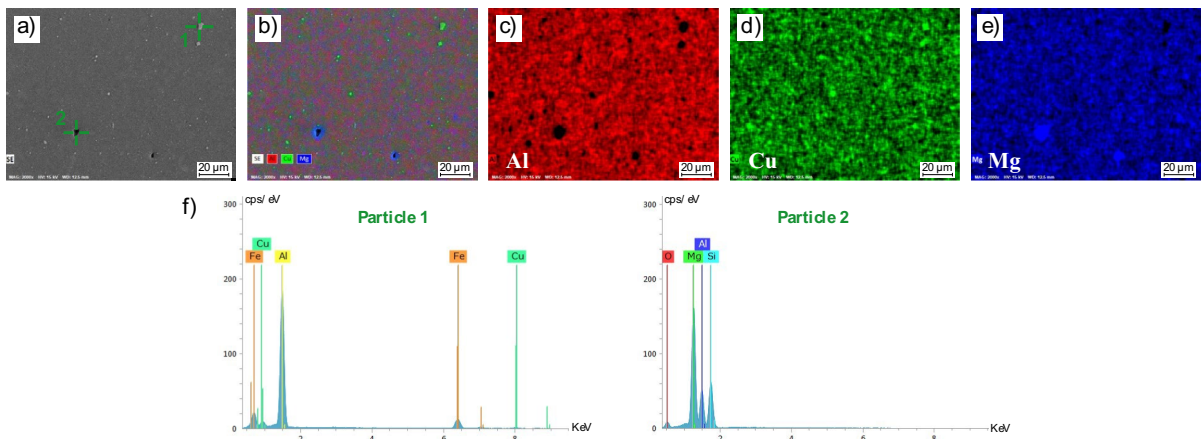
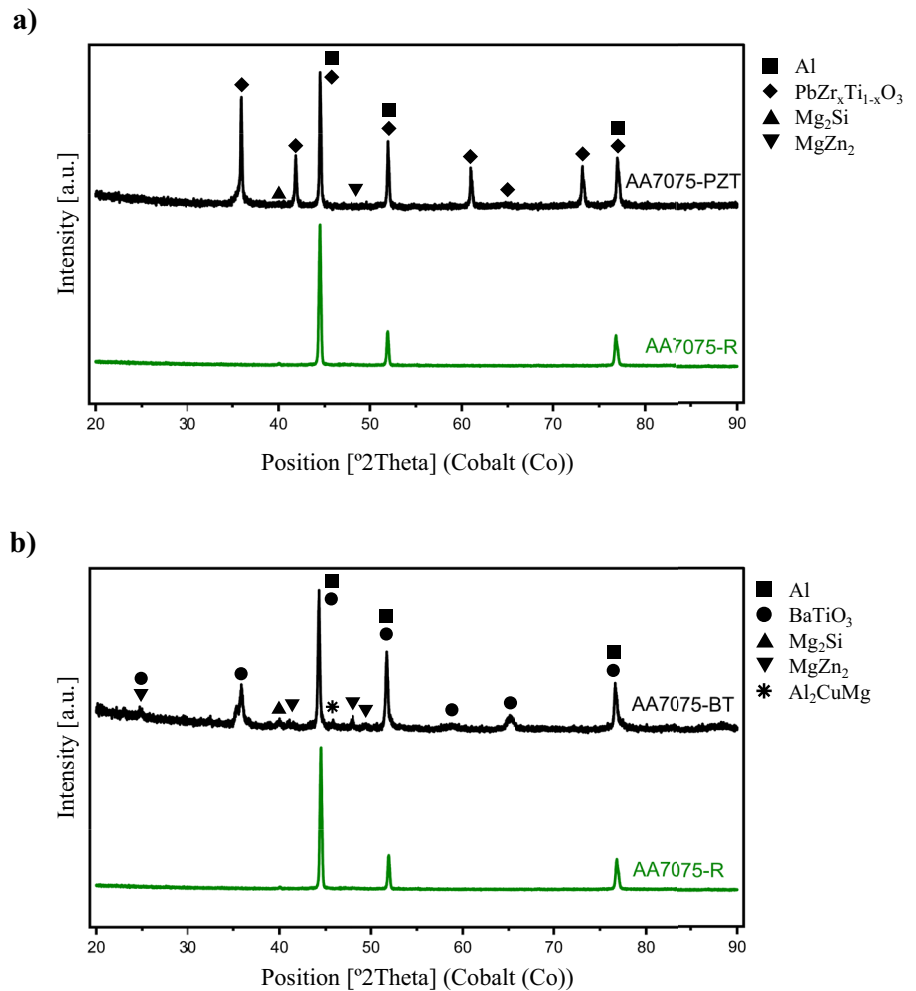


Fig. 11 SEM and EDX characterisation of particles' distribution of AA7075-R in zone influenced by the pin, at $\times 2000$ magnification

Fig. 12 XRD pattern of PSM incorporated with **a** PZT and **b** BT particles



(Fig. 11f) appears to be a precipitate of Al-Cu-Fe, namely $\text{Al}_7\text{Cu}_2\text{Fe}$, often seen in 7xxx series aluminium alloys and usually found with bar-like shapes in the base material. During the FSP thermal-mechanical cycle, these precipitates were broken up and then coarsened to spherical particles (Uzun 2007). The darker particle (particle 2) also seems to be a precipitate since the point spectrum analysis revealed mainly the presence of magnesium, silicon, and aluminium, similar to what was found in AA7075-PZT.

XRD examination of the processed sections of AA7075-PZT, AA7075-BT, and AA7075-R samples reveals the presence of BT and PZT particles in the nugget, as seen in Fig. 12. The XRD pattern for PZT (Fig. 12a) demonstrates the presence of PZT particles, which were recognized and indexed using a reference pattern analysed by Ferreira et al. (2023a). Figure 12a shows principal reflections (101) and (110) at 41.8° , as well as additional peaks.

The presence of BT particles in the nugget is clearly visible (Fig. 12b). Reflections at 24.8° are the tetragonal structure's (100) and (001) reflections. According to Ferreira et al. (2023a), the more powerful peaks at 35.9° correspond to the (101) and (011) reflections. It is worth noting that certain peaks correspond with the reflections off the aluminium plane.

XRD study of SSM's base material and processed area reveals the existence of piezoelectric particles in the stirred zone. Notably, the AA7075-T651 alloy's

strengthening precipitates, Al_2CuMg , Mg_2Si , and MgZn_2 , may be found in both pre- and post-processed areas (Inácio et al. 2022). This observation shows that the temperature obtained throughout the procedure was inadequate to cause the precipitates to dissolve. SEM/EDX investigations revealed and verified the existence of Mg_2Si precipitates.

3.3.2 Microcomputed tomography characterisation

Figure 13 shows the particle distribution as determined by μ -CT analysis. An inclusion analysis was also performed to determine the existence of internal agglomerates in the processing zone.

Figure 13a–e, f–j) show the findings for the AA7075 with BT and PZT particles, respectively. The PSM containing BT particles was found to exhibit tiny particle agglomerates in the nugget's center area along its length, in both the Y and Z directions. On the other hand, the incorporation of PZT into this alloy resulted in many more agglomerates within the nugget, with larger volumes, particularly in the top portion of the nugget on the retreating side.

Figure 14 presents a comparison of μ -CT data with PSM macrographs to better understand the relationship between inclusion analysis and agglomerates. This comparison reveals a higher concentration and greater presence of BT particle

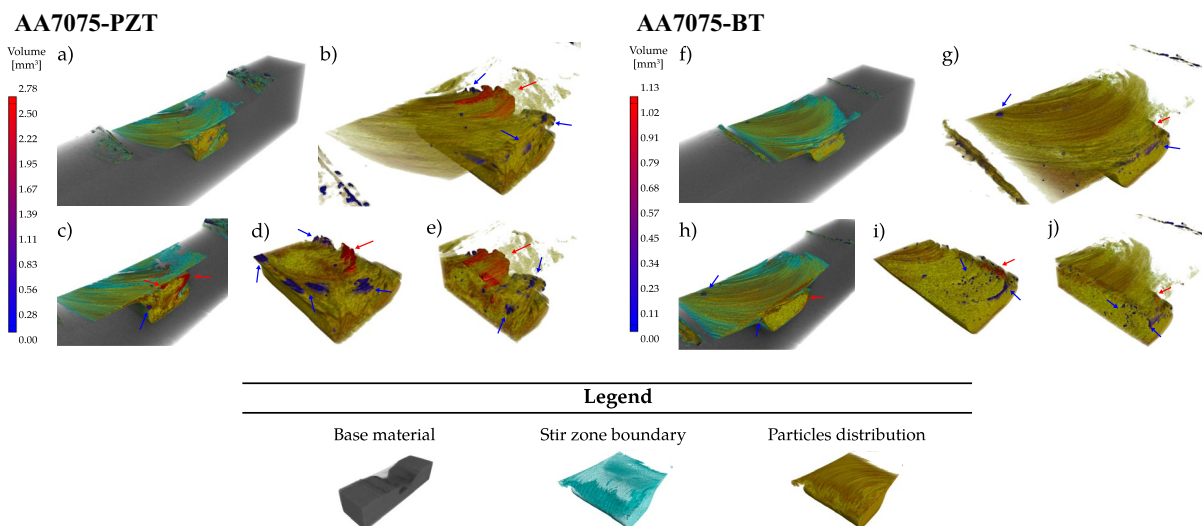


Fig. 13 μ -CT study of PSM: sample a, f; particles' distribution b, g; sample transverse cross section c, h, and nugget longitudinal cross section d, e, i, j

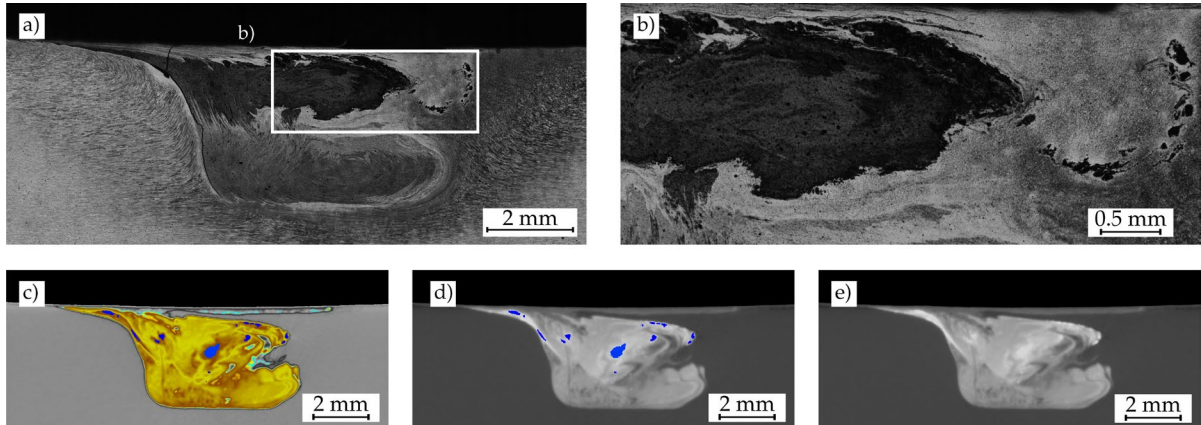
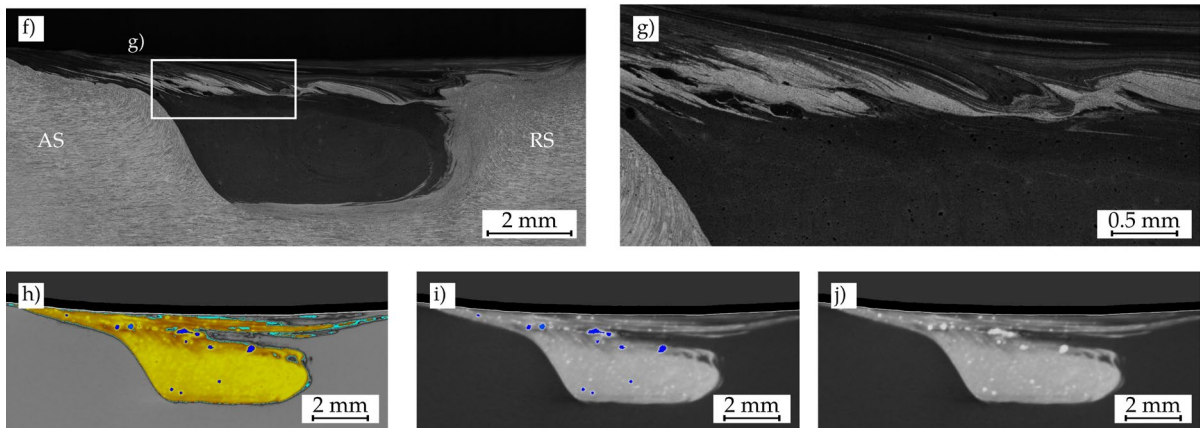
AA7075-PZT**AA7075-BT**

Fig. 14 Comparison of inclusion analyses and particle distribution in SSMs, shown through macrographs **a, f** and μ -CT images **c–e, h–j**. The colour scale used in the inclusion analysis is consistent with that in Fig. 13

agglomerates near the shoulder-affected zone in the AA7075-BT samples. It is also noted that the area influenced by the pin is characterized by a better distribution of particles and a lack of significant agglomerates. Additionally, the inclusion analysis allowed for the localization of particle agglomerates, which are identified by their white coloration, as depicted in Fig. 14j.

The AA7075-PZT sample's micrograph (see Fig. 14a, b) depicts two different regions inside the nugget, one upper region with darker colouration where it can be distinguished localised agglomerates of particles and a lower region less dark without visual indication of agglomerates. The μ -CT

images revealed that, indeed, agglomerates of particles can be found inside the upper region and can be distinguishable again by a brighter white colouration.

3.3.3 Uniaxial tensile tests

The engineering stress/strain curves was obtained using uniaxial tensile testing to evaluate the mechanical behaviour of the PSMs, as shown in Fig. 15a, b, 16a, b and 17a, b), while the corresponding fracture surfaces under SEM at various magnifications are shown in Fig. 15c, d, 16c, d and 17c, d. Table 6

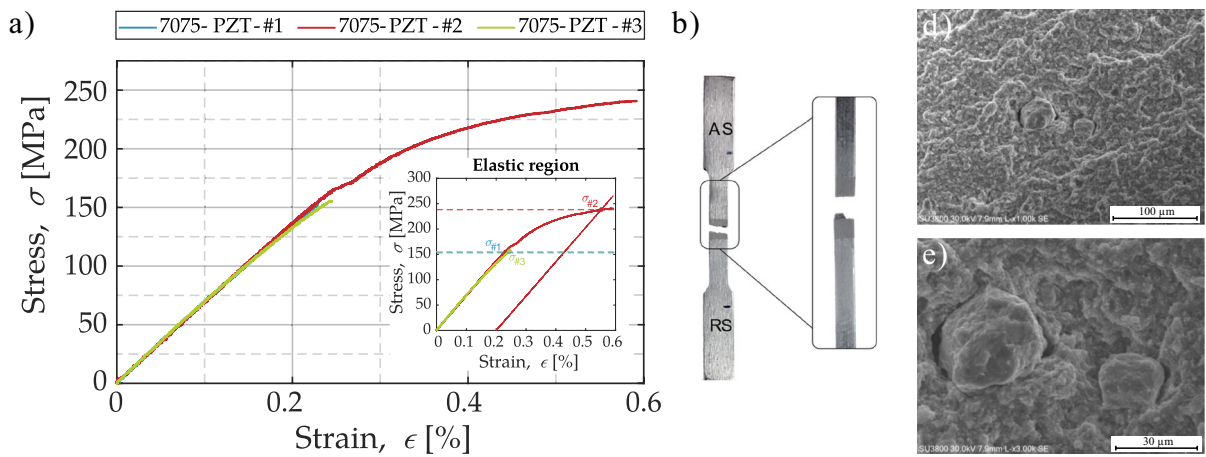


Fig. 15 Engineering stress–strain curves **a**, a cracked AA7075-PZT-#1 sample **b**, and a broken SSM surface **c**, **d** results of uniaxial tensile testing on AA7075-PZT

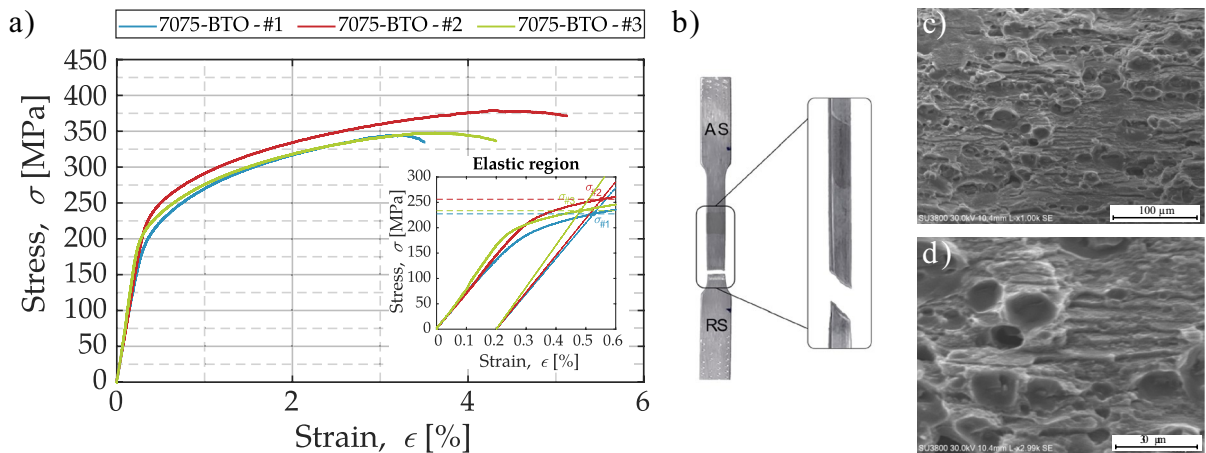


Fig. 16 Engineering stress–strain curves **a**, a cracked AA7075-BT-#1 sample **b**, and a broken SSM surface **c**, **d** results of uniaxial tensile testing on AA7075-BT

presents a summary of the mechanical qualities that were deemed most significant based on these testing.

It is possible to deduce that the yield strength ($\sigma_{0.2}$) of the material does not significantly change with the addition of particles by comparing with AA7075-R samples. Nevertheless, PZT particles addition yields a more brittle material (Fig. 15, 16) when compared to AA7075-BT samples. Since the elongation at fracture is much less for specimens containing PZT particles, this enhanced brittleness is clearly visible. PZT-containing specimens exhibit fractures only in the particle-rich areas, or stir zones, as seen in Fig. 15, which may indicate a weakened bond between the particles

and the aluminium matrix. Larger and more irregular PZT particle sizes are probably the cause of this poor bonding. As a result, the PZT particles do not effectively reinforce the matrix and may instead concentrate stresses, which can lower the yield strength.

The material containing PZT particles has lower ultimate tensile strength (σ_{UTS}) than AA7075-R. This decrease is ascribed to the increased brittleness generated by the delicate nature of the ceramic PZT particles, which fracture or detach from the matrix when loaded, impeding efficient stress transmission to the matrix. In the elastic zone, the material deforms evenly. However, when the material approaches

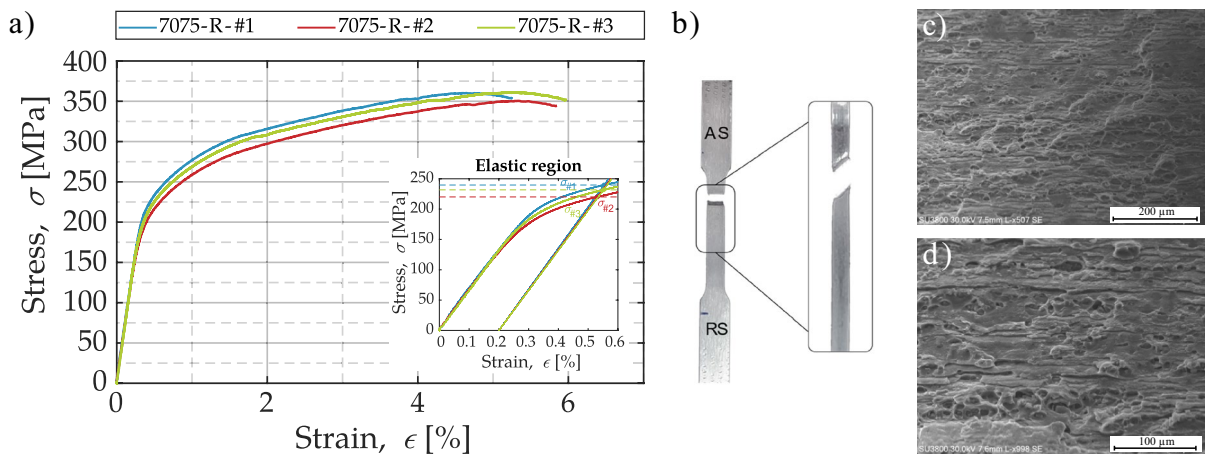


Fig. 17 Engineering stress–strain curves **a**, a cracked AA7075-R-#1 sample **b**, and a broken SSM surface **c**, **d** results of uniaxial tensile testing on AA7075-R

Table 6 Mechanical properties of AA7075-PZT, AA7075-BT and AA7075-R

Sample Reference	Yield strength, $\sigma_{0.2}$ [MPa]	Modulus of elasticity, E [GPa]	Ultimate tensile strength, σ_{UTS} [MPa]	Strain at fracture, ϵ_f
AA7075-PZT-#1	153.15	67.40	153.15	0.23
AA7075-PZT-#2	238.06	67.72	240.74	0.59
AA7075-PZT-#3	155.30	66.47	155.30	0.24
AA7075-BT-#1	227.36	69.73	344.56	3.51
AA7075-BT-#2	256.10	72.66	379.03	5.13
AA7075-BT-#3	233.60	82.78	347.53	4.32
AA7075-R-#1	239.71	67.91	360.23	5.26
AA7075-R-#2	220.09	66.48	350.47	5.85
AA7075-R-#3	231.75	65.88	360.76	5.98

the plastic area and the yield point, the deformation between the particles and the matrix becomes non-uniform, resulting in matrix fracture and fast crack propagation, as well as limited ductility. The AA7075-PZT material lacks ductility and hardening, therefore the σ_{UTS} is near to the yield strength, demonstrating its brittle properties.

In the AA7075 alloy, the fracture surfaces of these specimens exhibit not only well-developed dimples but also a few, although minimal, river marks. Consequently, the failure mode was primarily ductile, with the fracture surface occurring along planes at 45°. As shown in Fig. 16, the AA7075-BT fractured beside the processed zone, in base material, similar to the AA7075-R sample depicted in Fig. 17, leading to

the natural similarity between both fracture surfaces. Regarding the processing involving PZT particles (AA7075-PZT), where the fracture occurred within the processed zone, it is observed that the particles were the cause of the fracture mechanism. In other words, as the stir zone exhibits a high concentration of PZT particles, the aluminium walls between the particles became very thin. In this sequence, cracks can quickly form and propagate instantly (Nanoshel n.d. Nanoshel n.d. 2024). This results in minimal ductility, explaining why, in two out of three cases (Fig. 15a), the failure occurs within the elastic zone. Additionally, Fig. 15 suggests that the PZT particles are not fractured, which could indicate inadequate cohesion between the particles and the PSM matrix.

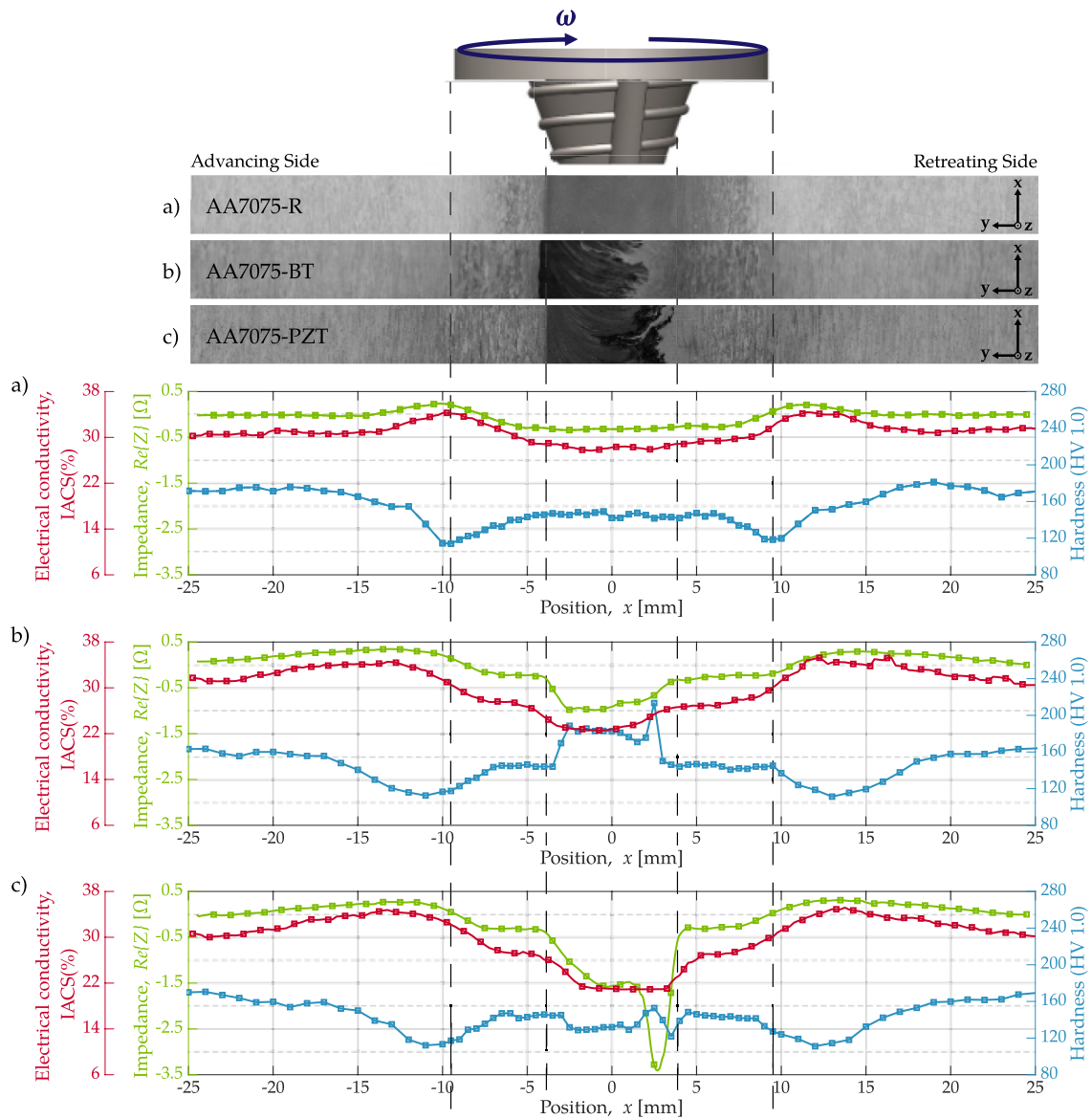


Fig. 18 Microhardness and electrical conductivity obtained from potential drop measurements and impedance changes obtained through eddy current testing of AA7075 samples

3.3.4 Microhardness and conductivity characterisation

A number of measurements were taken on the transverse section (Y direction) of the plates to describe both the processed and unprocessed sections of the AA7075 alloy and examine the particle distribution. Figure 18 depicts the results obtained for AA7075 alloy of microhardness and conductivity analyses.

The findings showed that because processed zones have more grain boundaries, which decrease electronic mobility and increase hardness, they have lower electrical conductivity. On the other hand, due to grain growth, the heat-affected zones displayed lower hardness and increased conductivity. In particular, the electrical conductivity is approximately 32 IACS (%) and the hardness is approximately constant at 170 HV1.0 on average in the unaffected

base material, which is in close agreement with the values of others authors (Vidal et al. 2022; Su et al. 2003) (175 HV and 33 IACS (%)). Grain coalescence caused the heat-affected zone to exhibit the highest electrical conductivity and lowest hardness; the processing's low annealing temperature lessened the T651 heat treatment's reinforcing impact.

Within the stir zones, a notable difference in hardness was observed between the types of particles used. Processing with BT particles resulted in a hardness increase of 60–100 HV1.0 compared to the base material, while processing with PZT particles led to a decrease in hardness by 40 HV1.0. This variation is attributed to the smaller size of BT particles, which enhances grain refinement, thus increasing hardness. In contrast, the larger size of PZT particles affects grain structure differently, resulting in decreased hardness. These observations are consistent with micrographs (Fig. 8) that show BT particles as significantly smaller than PZT particles. Overall, the changes in electrical conductivity and impedance measurements align well with the hardness profiles, confirming the coherence between the experimental results and theoretical expectations regarding the material's properties.

3.4 Sensorial properties evaluation

The PSM samples were subjected to cyclic mechanical loads while monitoring their electrical response to evaluate their sensorial properties. These tests involved applying repeated stresses to the samples at various frequencies, and the resulting electrical

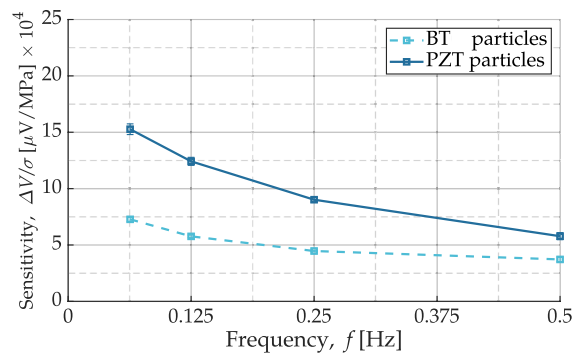


Fig. 20 Sensitivity of various piezoelectric particles in the AA7075 plates

characteristics were recorded. The experiments were conducted with different embedded piezoelectric particles, specifically BT and PZT, within an AA7075 aluminium alloy matrix. The results, illustrated in Fig. 19, demonstrate a consistent linear relationship between the applied stress and the electrical response. Notably, the sensitivity of the PSM samples was higher at lower loading frequencies, such as 0.063 Hz. This indicates that the materials exhibited greater responsiveness and a more pronounced electrical signal when subjected to slower, cyclic stresses. The AA7075-PZT achieved a maximum sensibility of $15.27 \times 10^{-4} \mu\text{V}/\text{MPa}$ when compared to AA7075-BT, which was 52% lower with a value of $7.28 \times 10^{-4} \mu\text{V}/\text{MPa}$.

An in-depth analysis will be conducted to clarify and establish conclusions regarding the results presented above. Figure 20 illustrates how the sensitivity

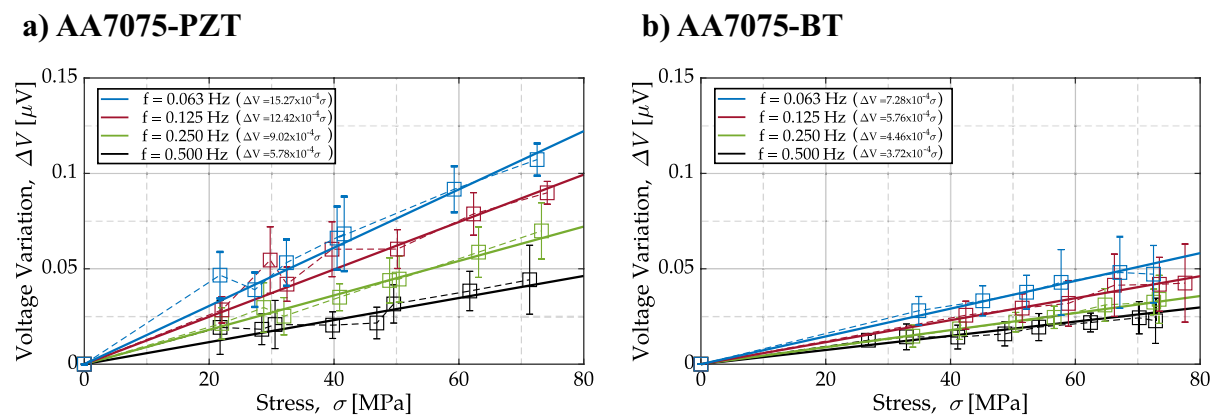


Fig. 19 Electrical response of the PSM to cyclic loads and varying frequencies

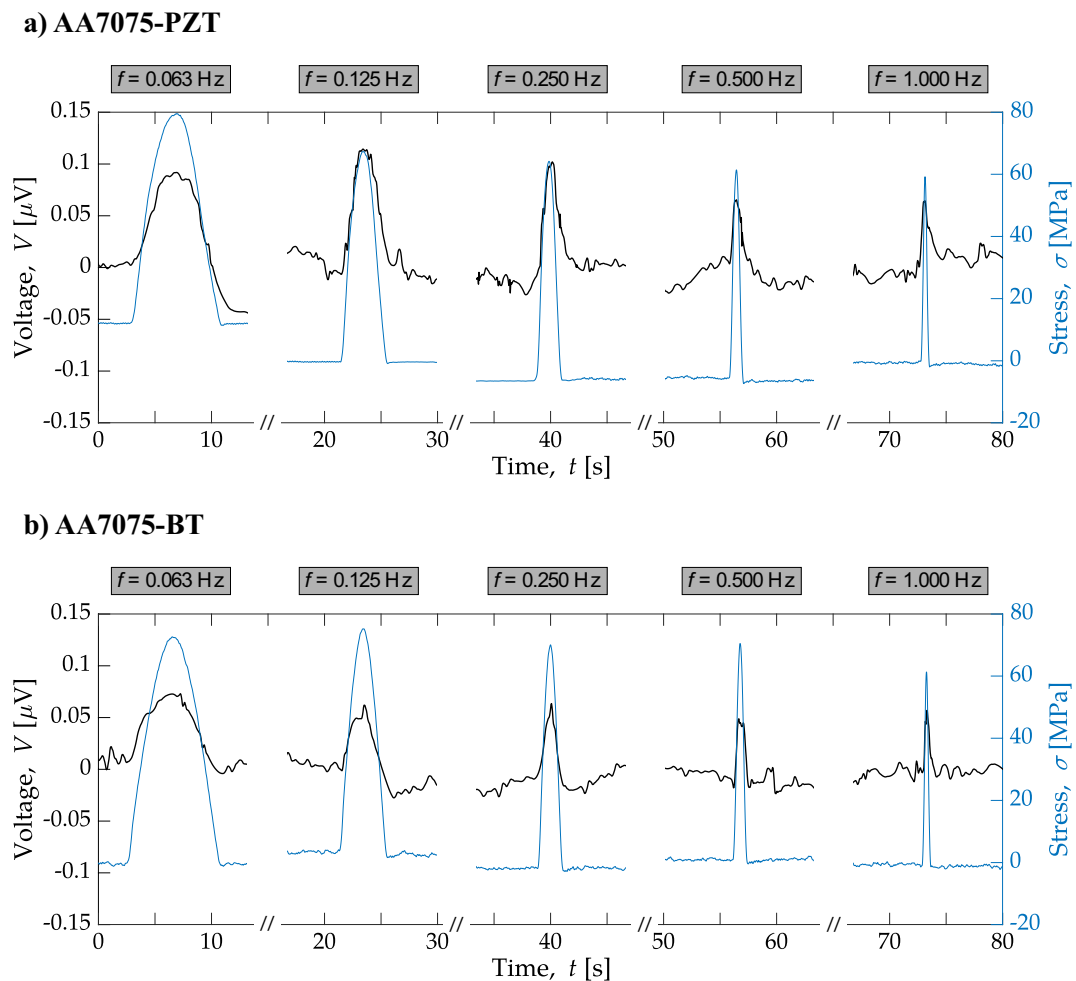


Fig. 21 Electrical response when the PSMs was subjected to a set of impulse loading

is affected by embedding BT and PZT piezoelectric particles inside the AA7075 matrix.

The results shown a clear tendency showing that incorporating PZT particles yields higher sensitivities compared to BT particles. This improved sensitivity can be attributed to the superior piezoelectric properties ($d_{33}/d_{31} = 270/-120$ pC/N) of PZT particles, compared to the $d_{33}/d_{31} = 190/-78$ pC/N of BT particles, as detailed in Table 3. Additionally, the graphics demonstrate a non-linear relationship between sensitivity and frequency, indicating that sensitivity does not change in a simple, linear fashion with varying frequencies but instead exhibits a more complex behaviour.

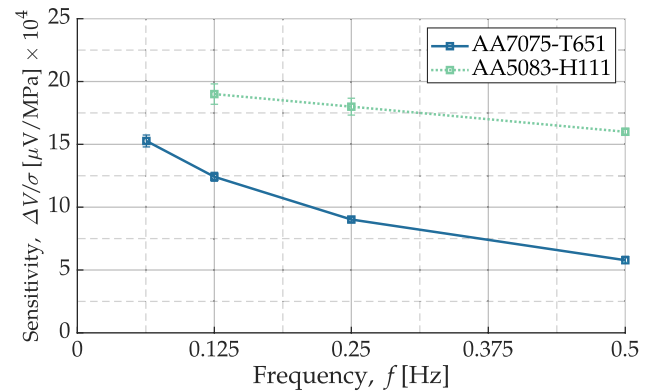
The Fig. 21 depicts the electrical response when the PSMs are exposed to a series of impulse loads.

The PSMs showed the predicted reactivity to these impulse loads, correctly reflecting the frequency of the applied loads and proving their capacity to detect changes in loading frequencies.

Figure 22 shows a comparison of sensitivity data for PSMs with PZT particles embedded in two different metallic matrices: AA7075-T651 and AA5083-H111 alloy. The AA7075-PZT samples outperformed that of the AA7075-BT samples, which was consistent with previous validations, due to the higher sensitivity of AA7075-PZT, as previous observed.

The comparison reveals that the sensitivity of the PZT particles embedded in the AA7075-T651 alloy was 30–60% lower than that in the AA5083-H111 alloy. Additionally, as the frequency increased, the

Fig. 22 Sensitivity for two aluminium matrices embedded with PZT particles



sensitivity gap between the two alloys became more pronounced.

4 Conclusion

This work effectively introduced sensory qualities to heat-treated AA7075-T651 by inserting piezoelectric particles, resulting in a PSM that can measure external loads. A linear connection between loads and electrical response of the PSMs was demonstrated during cyclic loading. Varying the frequency, the sensitivity of the PSMs exhibits a non-linear behaviour, increasing the sensibility as the frequency decreases and, therefore, making it more suitable for low-frequency applications. The AA7075-PZT achieved a maximum sensibility of $15.27 \times 10^{-4} \mu\text{V}/\text{MPa}$ when compared to AA7075-BT, which was 52% lower with a value of $7.28 \times 10^{-4} \mu\text{V}/\text{MPa}$. This maximum sensitivity was achieved applying cyclic loads with frequency of 0.063 Hz. Although PSMs are viable and offer a clear electrical voltage response, the component's mechanical behaviour must be ensured. Embedding piezoelectric particles in AA7075 resulted in a homogeneous distribution of particles in the nugget. However, the embedment of PZT particles in AA7075 proved challenging, where the stir zone presents two distinct regions with different particle distributions. The uniaxial tests revealed that embedding the piezoelectric particles increases the material's brittleness, especially regarding the embedment of PZT. The embedment with BT resulted in a primarily ductile fracture, with the fracture surface occurring along planes at 45° , exhibiting some evidence of river marks. The AA7075 aluminium matrices with

embedded PZT particles exhibited brittle fractures, characterized by cracks perpendicular to the applied load. Despite the poorer adhesion between PZT particles and the aluminium matrix compared to BT particles. This suggests that the stir zone's properties and weaker bonding contributed significantly to the brittle failure observed. The AA7075-PZT specimen fractured in the middle of the nugget. The hardness measurements allowed us to infer that embedding BT increased the hardness in the nugget compared to processing without the particles. Contrastingly, the embedment with PZT resulted in a decrease in hardness. This is following the micrographs and the fracture analysis that revealed larger agglomerates inside the stir zone and fractures occurring within this zone, indicating weaker bonding particles-metal matrix. The size and morphology of these particles showed irregularly shaped particles with a clear tendency to form agglomerates. Regarding the eddy current testing, both follow the registered hardness profiles and, therefore, contribute to characterising the particles' distribution and the impact of FSP on microstructure. The sensory characterization of the PSMs indicated an inverse connection between frequency and sensitivity, indicating that they are best suited for low-frequency applications. Also, the embedment of PZT particles provided generally better sensibilities than BT particles and their electrical response's potential varies linearly with the applied stress. As a result, it demonstrates that FSP is a remarkable technological approach for creating materials with sensorial properties, even though it changes the mechanical behaviour of the metal component after processing. In addition, despite generating low electric potential, these piezoelectric materials have significant applications

in structural health monitoring, vibration sensing, wearable technology, and energy harvesting. They can detect stress, strain, and vibrations for early failure detection and real-time monitoring, while also being useful in medical devices for sensing pressure changes. Additionally, their ability to harvest energy from low-level vibrations allows them to power small devices, highlighting their practical value even with limited voltage output.

Acknowledgements PMF also acknowledges FCT—Fundação para a Ciência e a Tecnologia for funding the PhD grant UI/BD/151055/2021. PMF, MAM, CV and MSC acknowledge FCT—Fundação para a Ciência e a Tecnologia for its financial support via projects UIDB/00667/2020 and UIDP/00667/2020 (UNIDEMI). FWCF acknowledges FCT—Fundação para a Ciência e a Tecnologia for funding the Ph.D. Grant 2022.13870.BD.

Author contribution Pedro M. Ferreira: Conceptualization, Methodology, Formal analysis, Investigation, Data curation, Writing- Original draft preparation, Visualization. David Caçador: Conceptualization, Methodology, Formal analysis, Writing- Reviewing and Editing. Miguel A. Machado: Conceptualization, Methodology, Formal analysis, Writing- Reviewing and Editing. Marta S. Carvalho: Conceptualization, Methodology, Formal analysis, Writing- Reviewing and Editing. Pedro Vilaça: Formal analysis, Writing- Reviewing and Editing. Gonçalo Sorger: Formal analysis, Writing- Reviewing and Editing. Francisco Werley Cipriano Farias: Formal analysis, Writing- Reviewing and Editing. Arthur Ribeiro Figueiredo: Formal analysis, Writing- Reviewing and Editing. Catarina Vidal: Conceptualization, Methodology, Formal analysis, Resources, Writing- Reviewing and Editing, Supervision, Project administration, Funding acquisition.

Funding Open access funding provided by FCTIFCCN (b-on). Open access funding provided by FCTIFCCN (b-on). FCT—Fundação para a Ciência e a Tecnologia, UI/BD/151055/2021, Pedro M. Ferreira, UIDP/00667/2020, UIDB/00667/2020, 2022.13870.BD, Francisco Werley Cipriano Farias.

Declarations

Conflict of interests The Authors declare that there is no conflict of interest.

Open Access This article is licensed under a Creative Commons Attribution 4.0 International License, which permits use, sharing, adaptation, distribution and reproduction in any medium or format, as long as you give appropriate credit to the original author(s) and the source, provide a link to the Creative Commons licence, and indicate if changes were made. The images or other third party material in this article are included in the article's Creative Commons licence, unless indicated otherwise in a credit line to the material. If material is not included in the article's Creative Commons licence and your

intended use is not permitted by statutory regulation or exceeds the permitted use, you will need to obtain permission directly from the copyright holder. To view a copy of this licence, visit <http://creativecommons.org/licenses/by/4.0/>.

References

- Anton, S.R., Sodano, H.A.: A review of power harvesting using piezoelectric materials (2003–2006). *Smart Mater. Struct.* **16**, R1–21 (2007). <https://doi.org/10.1088/0964-1726/16/3/R01>
- Askari, M., Brusa, E., Delprete, C.: Design and modeling of a novel multi-beam piezoelectric smart structure for vibration energy harvesting. *Mech. Adv. Mater. Struct.* **29**, 7519–7541 (2022). <https://doi.org/10.1080/15376494.2021.2001122>
- Bogue, R.: Smart materials: a review of capabilities and applications. *Assem. Autom.* **34**, 16–22 (2014). <https://doi.org/10.1108/AA-10-2013-094>
- Duarte, V.R., Rodrigues, T.A., Machado, M.A., Pragana, J.P.M., Pombinha, P., Coutinho, L., et al.: Benchmarking of nondestructive testing for additive manufacturing. *3D Print Addit Manuf.* **8**, 263–270 (2021). <https://doi.org/10.1089/3dp.2020.0204>
- Dwivedi, S.P., Sharma, S., Li, C., Zhang, Y., Kumar, A., Singh, R., et al.: Effect of nano-TiO₂ particles addition on dissimilar AA2024 and AA2014 based composite developed by friction stir process technique. *J. Market. Res.* **26**, 1872–1881 (2023). <https://doi.org/10.1016/j.jmrt.2023.07.234>
- Esther, L., Piselli, A., Faucheu, J., Delafosse, D., del Curto B.: Smart Materials: Development Of New Sensory Experiences Through Stimuli Responsive Materials. Institute of Network Cultures (2015)
- Ferreira, P.M., Machado, M.A., Carvalho, M.S., Vidal, C.: Embedded sensors for structural health monitoring: methodologies and applications review. *Sensors* **22**, 8320 (2022). <https://doi.org/10.3390/s22218320>
- Ferreira, P.M., Machado, M.A., Carvalho, M.S., Vidal, C.: Granting sensorial properties to metal parts through friction stir processing. *Measurement* (2023a). <https://doi.org/10.1016/j.measurement.2022.112405>
- Ferreira, P.M., Machado, M.A., Carvalho, M.S., Vilaça, P., Sorger, G., Pinto, J.V., et al.: Self-sensing metallic material based on PZT particles produced by friction stir processing envisaging structural health monitoring applications. *Mater Charact* **205**, 113371 (2023b). <https://doi.org/10.1016/j.matchar.2023.113371>
- Ferreira, P.M., Machado, M.A., Vidal, C., Carvalho, M.S.: Modelling electro-mechanical behaviour in piezoelectric composites: current status and perspectives on homogenisation. *Adv. Eng. Softw.* **193**, 103651 (2024a). <https://doi.org/10.1016/j.advengsoft.2024.103651>
- Ferreira, P.M., Meireles, A., Vidal, C., Carvalho, M.S., Machado, M.A.: Evaluation of self-sensing material behaviour: Insights from cyclic and pulse load testing. *Measurement* **234**, 114878 (2024b). <https://doi.org/10.1016/j.measurement.2024.114878>
- Ferreira, P.M., Caçador, D., Machado, M., Carvalho, M.S., Vilaca, P., Sorger, G., et al.: Enabling electrical response

- through piezoelectric particle integration in AA2017-T451 aluminium parts using FSP technology. *Smart Mater. Struct.* (2024c). <https://doi.org/10.1088/1361-665X/ad4d45>
- Gohari, S., Mozafari, F., Moslemi, N., Mouloudi, S., Alebrahim, R., Ahmed, M., et al.: Static and dynamic deformation response of smart laminated composite plates induced by inclined piezoelectric actuators. *J. Compos. Mater.* **56**, 3269–3293 (2022). <https://doi.org/10.1177/00219983221107257>
- Hussain, C.M., Di Sia, P. (eds.): *Handbook of Smart Materials, Technologies, and Devices*. Springer International Publishing, Cham (2020). <https://doi.org/10.1007/978-3-030-58675-1>
- Inácio, P.L., Nogueira, F., Ferreira, F.B., Vidal, C., Schell, N., Tero, T., et al.: Functionalized material production via multi-stack Upward Friction Stir Processing (UFSP). *Mater. Manuf. Processes* **37**, 11–24 (2022). <https://doi.org/10.1080/10426914.2021.1942909>
- Khan, M.A., Butola, R., Gupta, N.: A review of nanoparticle reinforced surface composites processed by friction stir processing. *J. Adhes. Sci. Technol.* **37**, 565–601 (2023). <https://doi.org/10.1080/01694243.2022.2037054>
- Lines, M.E., Glass, A.M.: *Principles and Applications of Ferroelectrics and Related Materials*. Oxford University Press (1979)
- Liu, S., Paidar, M., Mehrez, S., Ojo, O.O., Mahariq, I., Elbadawy, I.: Development of AA6061/316 stainless steel surface composites via friction stir processing: effect of tool rotational speed. *Mater. Charact.* **192**, 112215 (2022). <https://doi.org/10.1016/j.matchar.2022.112215>
- Mahapatra, S.D., Mohapatra, P.C., Aria, A.I., Christie, G., Mishra, Y.K., Hofmann, S., et al.: Piezoelectric materials for energy harvesting and sensing applications: roadmap for future smart materials. *Adv. Sci.* (2021). <https://doi.org/10.1002/advs.202100864>
- Manroo, S.A., Khan, N.Z., Ahmad, B.: Study on surface modification and fabrication of surface composites of magnesium alloys by friction stir processing: a review. *J. Eng. Appl. Sci.* **69**, 25 (2022). <https://doi.org/10.1186/s44147-022-00073-9>
- Mateus, R., Pinto, A., Pereira, J.M.C.: Dynamics of thermal plumes for large spaces: a comparative study of in-situ smoke test and a CFD model. *Energy Build.* **319**, 114512 (2024a). <https://doi.org/10.1016/j.enbuild.2024.114512>
- Mateus, R., Pinto, A., Pereira, J.M.C.: Natural ventilation in large spaces: CFD simplified model validated with full-scale experimental data of Roman Baths. *Build. Environ.* **266**, 112077 (2024b). <https://doi.org/10.1016/j.buildenv.2024.112077>
- Mehdi, M.E.M., Qaiss el kacem, A., Bouhfid, R.: Introduction: Different Types of Smart Materials and Their Practical Applications. In: *Polymer Nanocomposite-Based Smart Materials*, pp. 1–19. Elsevier (2020). <https://doi.org/10.1016/B978-0-08-103013-4.00001-7>
- Moreira, F., Ferreira, P.M., Silva, R.J.C., Santos, T.G., Vidal, C.: Aluminium-based dissimilar alloys surface composites reinforced with functional microparticles produced by upward friction stir processing. *Coatings* **13**, 962 (2023). <https://doi.org/10.3390/coatings13050962>
- Mou, C., Saffari, P., Li, D., Zhou, K., Zhang, L., Soar, R., et al.: Smart structure sensors based on embedded fibre Bragg grating arrays in aluminium alloy matrix by ultrasonic consolidation. *Meas. Sci. Technol.* **20**, 034013 (2009). <https://doi.org/10.1088/0957-0233/20/3/034013>
- Nanoshel. <https://www.nanoshel.com/sections/nanopowder-compounds> (2024) Accessed 4 August 2024
- Oyedepo, S.O., Dirisu, J.O., Udoye, N.E., Fayomi, O.S.I.: Progresses on Green and Smart Materials for Multifaceted Applications. In: Hussain, C.M., Di Sia, P. (eds.) *Handbook of Smart Materials, Technologies, and Devices*, pp. 1439–1466. Springer International Publishing, Cham (2022). https://doi.org/10.1007/978-3-030-84205-5_41
- Parumandla, N., Adepu, K.: Effect of Al₂O₃ and SiC nano reinforcements on microstructure, mechanical and wear properties of surface nanocomposites fabricated by friction stir processing. *Mater. Sci.* (2018). <https://doi.org/10.5755/j01.ms.24.3.18220>
- Ragunath, S., Radhika, N., Aravind Krishna, S., Jeyaprakash, N.: Synthesis of high entropy alloy for surface modification by friction stir process: recent advances and future directions. *Met. Mater. Int.* **30**, 1170–1199 (2024). <https://doi.org/10.1007/s12540-023-01584-7>
- Ramanathan, A.K., Gingerich, M.B., Headings, L.M., Dapino, M.J.: Metal structures embedded with piezoelectric PVDF sensors using ultrasonic additive manufacturing. *Manuf. Lett.* **31**, 96–100 (2022). <https://doi.org/10.1016/j.mfglet.2021.08.001>
- Rendas, P., Imperadeiro, A., Martins, R.F., Soares, B.A.R.: High-cycle fatigue behaviour of polyetheretherketone (PEEK) produced by additive manufacturing. *Polymers* **16**, 18 (2023). <https://doi.org/10.3390/polym16010018>
- Rendas, P., Figueiredo, L., Melo, P., Galhano, C., Vidal, C., Soares, B.A.R.: Investigation of friction stir welding of additively manufactured biocompatible thermoplastics using stationary shoulder and assisted heating. *Polymers* **16**, 1897 (2024). <https://doi.org/10.3390/polym16131897>
- Santos, T.G., Miranda, R.M., Vilaça, P., Teixeira, J.P., dos Santos, J.: Microstructural mapping of friction stir welded AA 7075–T6 and AlMgSc alloys using electrical conductivity. *Sci. Technol. Weld. Joining* **16**, 630–635 (2011). <https://doi.org/10.1179/1362171811Y.0000000052>
- Santos, T.G., Oliveira, J.P., Machado, M.A., Inácio, P.L., Duarte, V.R., Rodrigues, T.A., et al.: Reliability and NDT Methods. In: Marques, A.T., Esteves, S., Pereira, J.P.T., Oliveira, L.M. (eds.) *Additive Manufacturing Hybrid Processes for Composites Systems*, pp. 265–295. Springer International Publishing, Cham (2020). https://doi.org/10.1007/978-3-030-44522-5_8
- Sattari, B., Shamanian, M., Salimijazi, F., Salehi, M.: Surface modification by friction stir processing of low-carbon steel: microstructure investigation and wear performance. *J. Mater. Eng. Perform.* **27**, 751–763 (2018). <https://doi.org/10.1007/s11665-017-3087-7>
- Scheffler, S., Poulin, P.: Piezoelectric fibers: processing and challenges. *ACS Appl. Mater. Interfaces* **14**, 16961–16982 (2022). <https://doi.org/10.1021/acsami.1c24611>
- Selleri, G., Gino, M.E., Brugo, T.M., D’Anniballe, R., Tabucol, J., Focarete, M.L., et al.: Self-sensing composite material based on piezoelectric nanofibers. *Mater. Des.* **219**,

- 110787 (2022). <https://doi.org/10.1016/j.matdes.2022.110787>
- Sezer, N., Koç, M.: A comprehensive review on the state-of-the-art of piezoelectric energy harvesting. *Nano Energy* **80**, 105567 (2021). <https://doi.org/10.1016/j.nanoen.2020.105567>
- Sharma, A.: Effect of porosity on active vibration control of smart structure using porous functionally graded piezoelectric material. *Compos. Struct.* **280**, 114815 (2022). <https://doi.org/10.1016/j.compstruct.2021.114815>
- Sobczyk, M., Wiesenhütter, S., Noennig, J.R., Wallmersperger, T.: Smart materials in architecture for actuator and sensor applications: a review. *J. Intell. Mater. Syst. Struct.* **33**, 379–399 (2022). <https://doi.org/10.1177/1045389X211027954>
- Sorger, G.L., Oliveira, J.P., Inácio, P.L., Enzinger, N., Vilaça, P., Miranda, R.M., et al.: Non-destructive microstructural analysis by electrical conductivity: comparison with hardness measurements in different materials. *J. Mater. Sci. Technol.* **35**, 360–368 (2019). <https://doi.org/10.1016/j.jmst.2018.09.047>
- Su, J.-Q., Nelson, T.W., Mishra, R., Mahoney, M.: Microstructural investigation of friction stir welded 7050–T651 aluminum. *Acta Mater.* **51**, 713–729 (2003). [https://doi.org/10.1016/S1359-6454\(02\)00449-4](https://doi.org/10.1016/S1359-6454(02)00449-4)
- Thermo Fisher Scientific: <https://www.thermofisher.com/order/catalog/product/0%0A88267.36?SID=srchsrp-088267.22> (2024) Accessed 4 August 2024
- Uzun, H.: Friction stir welding of SiC particulate reinforced AA2124 aluminium alloy matrix composite. *Mater. Des.* **28**, 1440–1446 (2007). <https://doi.org/10.1016/j.matdes.2006.03.023>
- Vidal, C., Alves, P., Alves, M.M., Carmezim, M.J., Fernandes, M.H., Grenho, L., et al.: Fabrication of a biodegradable and cytocompatible magnesium/nanohydroxyapatite/fluorapatite composite by upward friction stir processing for biomedical applications. *J. Mech. Behav. Biomed. Mater.* **129**, 105137 (2022). <https://doi.org/10.1016/j.jmbbm.2022.105137>
- Vidal, C., Ferreira, P.M., Ferreira, F.B., Buinho, M., Silva, T.T., Santos, T.G.: Improving the stability of the friction stir channelling technology via a cooled copper backing plate. *Int. J. Adv. Manuf. Technol.* (2023a). <https://doi.org/10.1007/s00170-023-12211-5>
- Vidal, C., Ferreira, P.M., Inácio, P.L., Ferreira, F.B., Santiago, D., Meneses, P., et al.: Particles' distribution enhancing in aluminum-based composites produced by upward friction stir processing. *Int. J. Adv. Manuf. Technol.* **127**, 2745–2757 (2023b). <https://doi.org/10.1007/s00170-023-11664-y>
- Wu, T., Zhao, F., Luo, H., Wang, H., Li, Y.: Temperature monitoring and material flow characteristics of friction stir welded 2A14-t6 aerospace aluminum alloy. *Materials* **12**, 3387 (2019). <https://doi.org/10.3390/ma12203387>
- Wu, B., Ibrahim, M.Z., Raja, S., Yusof, F., Abdulrazak, B., Binmuhamad, M.R., et al.: The influence of reinforcement particles friction stir processing on microstructure, mechanical properties, tribological and corrosion behaviors: a review. *J. Mater. Res. Technol.* **20**, 1940–1975 (2022). <https://doi.org/10.1016/j.jmrt.2022.07.172>
- Xi, X., Chung, D.D.L.: Piezoresistivity and piezoelectricity discovered in aluminum, with relevance to structural self-sensing. *Sens. Actuators A Phys.* **289**, 144–156 (2019). <https://doi.org/10.1016/j.sna.2019.02.013>
- Yanaseko, T., Asanuma, H., Sato, H.: Characterization of a metal-core piezoelectric ceramics fiber/aluminum composite. *Mech. Eng. J.* **2**, 14-00357–14-00357 (2015). <https://doi.org/10.1299/mej.14-00357>
- Yanaseko, T., Sato, H., Narita, F., Kuboki, I., Asanuma, H.: Improvement estimation accuracy of impact detection using metal-core piezoelectric fiber/aluminum composites. *Adv. Eng. Mater.* (2019). <https://doi.org/10.1002/adem.201900550>

Publisher's Note Springer Nature remains neutral with regard to jurisdictional claims in published maps and institutional affiliations.